

The following pages report the document:

A. Amicarelli, 2024, A Lagrangian RANS CFD-SPH code for turbulent flows with pollutant transport and applications to Outdoor/Indoor/Duct Air Quality, paper preprint, protocol RS2401, pp.1-30.

A Lagrangian RANS CFD-SPH code for turbulent flows with pollutant transport and applications to Outdoor/Indoor/Duct Air Quality

paper preprint, protocol RS2401; Copyright 2024 (Andrea Amicarelli)
author: Andrea Amicarelli, freelance, Lucca, Italy, andrea.amicarelli@gmail.com

Abstract (max.150 words)

A Lagrangian RANS CFD-SPH code for turbulent flows and pollutant dispersion relies on Kato & Launder's improved k- ϵ s model, the mean-concentration Balance Equation BE and the Weakly-Compressible approach, with turbulent transport term in the Continuity Equation. Peculiar time schemes and numerical solutions, including a stabilization term for the Momentum Equation and a shell SPH filter, stabilize BEs and satisfy physical constraints minimizing accuracy loss. Specific Wall Functions apply. A SPH Time-Space Ensemble filter preserves the correctness of the ensemble statistics. The code (CFD-OUT-sweePDF v.1.0.0, Amicarelli et al.) is validated by comparison with experiments and closed-form solutions under: grid turbulence with surface Pollutant Source PS; experimental shear flow with Elevated PS; experimental confined flow past a wall-mounted cubic obstacle with Canyon PS. The investigated applications are Outdoor/Indoor/Duct Air Quality. On the transporting flow, the performance level reaches the state-of-the-art RANS-FVM codes, which use more nodes by a factor of 5, and is limitedly inferior to LES-FVM, featured by much larger costs and more statistics.

Keywords (max.6): RANS SPH; mean concentration; CFD-OUT-sweePDF; air quality; SPH time schemes; SPH Time-Space Ensemble filter.

1. INTRODUCTION

Among the Computational Fluid Dynamics (CFD) methods for turbulent flows, Smoothed Particle Hydrodynamics (SPH) has shown several advantageous features: Lagrangian modelling (e.g., free and exact advection terms; direct assessment of interfaces between fluids or phases); explicit time integration under Weakly-Compressible (WC) approach; independent particle Partial Differential Equations (PDEs); meshless method; suitability for multi-physics (e.g., transport of solid bodies in fluid flows); versatility in scheme coupling. On the other hand, the main SPH shortcomings vs. mesh-based CFD methods are the multi-resolution complexity, the difficulty in formally achieving high consistency orders and the crowded computational stencil. A synthetic and non-exhaustive state of the art on turbulence SPH models is discussed hereafter, considering the following categories:

- ILES-SPH (Implicit Large Eddy Simulation - SPH). The vast majority of SPH studies implicitly consider turbulence by means of explicit numerical diffusion terms in the Momentum Equation (ME), i.e., the SPH artificial-viscosity term (Monaghan, 1992, [1]), and in the Continuity Equation (CE) in case of WC-SPH models.
- MILES-SPH (Monotone Integrated LES - SPH). MILES models (e.g., Boris et al., 1992, [2]) are based on Godunov-type schemes, spatial reconstruction schemes (e.g., MUSCL) and Riemann Solvers or Lax-Friedrichs terms. MILES implicitly represents LES-filtered quantities. Sub-Grid (SG) terms are implicitly modelled via physically based spatial reconstructions, not involving the SG Turbulent Kinetic Energy (TKE). MILES-SPH models (e.g., Vacondio, 2011, [3]) stagger in space the divergence and the gradient operators to avoid their colocation, thus increasing the stability domain. SPH-ALE (Arbitrary Lagrangian-Eulerian) models (e.g., Marongiu et al., 2010, [4]; Koukouvinis et al., 2013, [5]) are often examples of MILES-SPH solutions. The diffusion term of Ferrari et al. (2009, [6]) can be interpreted as a SPH-MILES term for CE.
- SGS-LES (Sub-Grid-Scheme-LES) SPH. Although LES-SPH is featured by double spatial resolution, i.e., the particle and the filter sizes, the explicit LES-SPH models represent Reynolds' stress (RS) tensor and neglect Leonards' and the cross stress tensors. From this viewpoint, they act as SGS (or Sub-Particle Schemes) more than Sub-Filter Schemes (SFS). The "delta-SPH" term in Antuono et al. (2012, [7]) is an example of SGS-LES term in CE. Di Mascio et al. (2017, [8]) introduced a deconvolution method in SPH to distinguish between unfiltered instantaneous-

like quantities and LES-filtered quantities. Some SGS-LES SPH models adopted a strategy merging SGS Smagorinsky's model, SPH deconvolution terms and a SGS diffusion term in CE (e.g., Meringolo et al., 2018, [9]; Sun et al., 2019, [10]). Smagorinsky's model was also used in Gotoh & Sakai (2006, [11]), Lo & Shao (2002, [12]), Ren et al. (2014, [13]), Sigalotti et al. (2021, [14]), Isik & He (2021, [15]), Shi & Huang (2022, [16]), and Okraschevski et al. (2022, [17]).

- RANS (Reynolds-Averaged Navier-Stokes) k- ϵ s SPH. Violeau & Issa (2007, [18]) presented a RANS k- ϵ s SPH solution, with a semi-linear model for the mean-TKE production rate. Ferrand et al. (2013, [19]) used Wall Functions (WFs) for the slip coefficient and the mean-TKE dissipation rate. Leroy et al. (2014, [20]) presented a 2D k- ϵ s Incompressible-SPH (ISPH) model with the TKE-gradient term in RANS-ME. Peculiar time schemes for the Balance Equations (BEs) of the mean-TKE (TKE-BE) and its dissipation rate (ϵ -BE) were presented. A k- ϵ s SPH model for river hydraulics was validated under hydraulic jumps (De Padova et al., 2017, [21]).
- RANS RS- ϵ s SPH. Violeau & Issa (2007, [18]) also presented a simplified 2nd-order turbulence SPH model mentioned as “algebraic” Reynolds-stress (RS) model.
- RANS-PDF (Probability Density Function). Welton & Pope (1997, [22]) discretized RANS-PDF Stochastic Differential Equations (SDEs) by SPH. Another validation is available in Canor & Denoël (2013, [23]). This approach might suffer from numerical instabilities, as the trajectories of the computational nodes mimic the chaotic trajectories of fluid particles, and might need relevant computational resources for proper time schemes, stabilization and/or ALE terms.
- DNS (Direct Numerical Simulation) - SPH. Mayrhofer et al. (2015, [24]) reproduced a minimum flow unit in a “quasi-DNS” SPH simulation.

SPH studies on the turbulent transport of a scalar in a fluid flow seem rare or absent. Considering any numerical method, some of the most advanced and affordable approaches are listed hereafter:

- RANS Balance Equations along the mean-velocity trajectory (e.g., Efthimiou et al., 2017, [25]). These models are featured by: the assessment of the concentration ensemble mean and rarely of the concentration ensemble variance; no effect of velocity autocorrelation; limited accuracy for second-order kinetics; a sole set of computational nodes for the transporting fluid and the scalar.
- RANS-LSM (Lagrangian Stochastic Models or macro-mixing models, Thomson, 1987, [26]), with: instantaneous-like quantities; SDEs for velocity and the scalar; coherence with velocity autocorrelation; concentration ensemble mean; micro-mixing scheme for other ensemble statistics and accurate second-order kinetics; dependency on velocity pdfs; input velocity statistics.
- RANS-SPDF (Scalar PDF). This is based on SDEs for the trajectory and the scalar (e.g., Haworth, 2010, [27]), with: instantaneous-like quantities; scalar ensemble statistics and pdf; no effect of velocity autocorrelation; limited accuracy for second-order kinetics; input velocity statistics.
- RANS-PDF (e.g., Pope, 1985, [28]). Its reference variant (VSPDF) have SDEs for velocity and the scalar, featuring: instantaneous-like quantities; simultaneous assessment of any ensemble statistic and the pdf of both velocity and the scalar; coherence with velocity autocorrelation, RANS Reynolds' stress Balance Equation (RS-BE) and TKE-BE; accurate second-order kinetics and high-order scalar statistics; two sets of computational nodes (Particle-in-Cell approach).
- Balance Equation for LES-filtered concentration along the LES-filtered-velocity trajectory, with deterministic SGS (e.g., Meeder & Nieuwstadt, 2000, [29]), featured by: LES-filtered concentration statistics; no effect of SG velocity autocorrelation; limited accuracy for second-order kinetics; sole set of computational nodes for the transporting fluid and the scalar.
- Balance Equation for LES-filtered concentration, with stochastic SGS (e.g., Vinkovic et al., 2006, [30]): it is the LES equivalent of coupling LSM with a RANS model for the transporting fluid, provided that the LES-filtered statistics replace the ensemble statistics.
- SFDF (Scalar Filtered Density Function; Haworth, 2010, [27]): the LES version of RANS-SPDF.
- FDF (e.g., Gicquel et al., 2002, [31]), or LES-PDF: the LES equivalent of RANS-PDF.

With the aims of modelling both turbulent flows and pollutant dispersion, adopting the fastest and cheapest approach among the most accurate ones, exploiting the SPH advantages and using a sole set

of computational nodes, the code CFD-OUT-sweePDF v.1.0.0 (Sec.2) was written. It is a Lagrangian RANS “Kat&Lau-k-eps” CFD-SPH code with BE for the concentration ensemble mean. Peculiar numerical solutions stabilize the model and respect the physical BE constraints with minimum loss of accuracy (Sec.3). The code WFs are reported in Sec.4. Validations refer to grid turbulence with surface Pollutant Source (PS, Sec.5), an experimental shear flow with Elevated PS (Sec.6) and a confined flow past a wall-mounted cubic obstacle with Canyon PS (Sec.7). Associated applications refer to air-treatment processes (Sec.5), Outdoor Air Quality (OAQ, Sec.6) and Indoor Air Quality (IAQ, Sec.7). The novelties of the study are cited in the abstract and in Sec.8. The following information regards all the test cases above. As the experimental temperature T (K) is unavailable, the fluid reference density $\rho_{ref}=1.20\text{kg/m}^3$ and dynamic viscosity $\mu=1.81\times10^{-5}\text{Pa}\times\text{s}$ are representative of air at ambient conditions. Simulations are executed under reduced pressure for barotropic neutrally-buoyant micro-scale airflows (Amicarelli, 2024, [32]). Initial Conditions (IC) are set as follows: the stream-wise mean velocity assumes the minimum value among the inlet SPH particles; the selected particle also sets the other IC values, except for the mean concentration, which is null. Stationary conditions are achieved at the end of a transient period upon satisfaction of a convergence criterion based on the SPH-TSE filter (Sec.2); no IC node is present in the domain at validation time.

2. THE CODE CFD-OUT-SWEEPpdf V.1.0.0

CFD-OUT-sweePDF v.1.0.0 (Amicarelli et al.) is a Lagrangian RANS CFD-SPH code with scalar ensemble mean for fluid flows around buildings/obstacles, at small Mach numbers. It has been applied to the following micro-scale air-quality applications: Outdoor Air Quality (OAQ), Indoor Air Quality (IAQ), air-treatment processes. The code adopts the WC approach to assess the mean pressure and relies on Kato & Launder’s k-eps model (Kat&Lau-k-eps), being considered one of the two most accurate 2-equation 1st-order turbulence closures with Realizable k-eps (R.k-eps). The semi-implicit Euler’s scheme and peculiar variants of the forward-backward Euler’s scheme rule time integration, merging a spatial linear filter, a stabilization term for the Momentum Equation and the shell SPH filter to enhance the stability domains. The SPH Time-Space Ensemble (SPH-TSE) filter improves the accuracy of the ensemble statistics under specific conditions. Alternative Implicit LES (ILES-SPH) and Navier-Stokes (NS-SPH) formulations are available. The code can reproduce any useful spatial resolution under a maximum domain of $2\text{km}\times2\text{km}\times0.5\text{km}$. Formal details on the code are cited at the end of the document. A synthetic view of the code is presented in the following.

The application of the SPH filters $\langle \rangle$ and the semi-implicit Euler’s scheme to the RANS Momentum Equation (RANS-ME) and the Trajectory Equation (TE), traced by the mean motion of the computational particle “ \hat{o} ”, provides the following PDE scheme:

$$\underline{\hat{u}}_{0,k+1} = \underline{\hat{u}}_{0,k} + \left\{ \begin{array}{l} \frac{\underline{g}}{\underline{\rho}_0} - \frac{1}{3} \langle \nabla \bar{p} \rangle_{C1,0} - \frac{2}{3} \langle \nabla \bar{q} \rangle_{C1,0} + \\ + \left\langle \nabla \cdot \left[(\nu_T + \bar{\nu}) (\nabla \otimes \underline{\hat{u}})^T \right] \right\rangle_{C0,0} + \\ - 2 \max \left\{ \left(\frac{\bar{p}_0}{\underline{\rho}_0} + \frac{2}{3} \bar{q}_0 \right); 0 \right\} \langle \nabla 1 \rangle_{C-1,0} \end{array} \right\}_k \Delta t_k, \quad \underline{x}_{0,k+1} = \underline{x}_{0,k} + \underline{\hat{u}}_{0,k+1} \Delta t_k \quad (2.1)$$

where $\underline{\hat{u}}$ (m/s) is the mean velocity, \underline{g} (m/s²) is the gravitational acceleration, \bar{p} (kg×m⁻¹×s⁻²) is the mean pressure, $\underline{\rho}$ (kg/m³) is the mean density, \bar{q} (m²/s²) is the mean TKE, ν_T (m²/s) is the turbulent viscosity, $\bar{\nu}$ (m²/s) is the mean kinematic viscosity, t (s) is time, Δt (s) is the time step duration, the subscript “ k ” indicates the time step and \underline{x} (m) is the particle position. The last term within curly brackets is called “ME stabilization term”, for sake of simplicity.

The SPH filters and the forward-backward Euler's scheme with linear filter applies to RANS Continuity Equation (RANS-CE) as follows:

$$\begin{aligned}\bar{\rho}_{0,k+1,PRE} &= \bar{\rho}_{0,k} + \left[-\bar{\rho}_{0,k} \left\langle \nabla \cdot \bar{u} \right\rangle_{C1,0,k+1} + \left\langle \nabla \cdot (\nu_{T,k+1} \nabla \bar{\rho}_k) \right\rangle_{C0,0} \right] \Delta t_k, \\ \bar{\rho}_{0,k+1} &= (1 - \theta_{0,k+1}) \bar{\rho}_{0,k+1,PRE} + \theta_{0,k+1} \left\langle \bar{\rho}_{k+1,PRE} \right\rangle_{C0,0}, \quad \theta_{k+1} = \frac{\left(c_1 \frac{c_{ref}}{h} - 2 \frac{c_2 V_{T,k+1}}{h^2} \right) \Delta t_k}{(1 - W_{k+1} \omega_{k+1}) \left(1 + c_1 \frac{c_{ref}}{h} \Delta t_k \right) - 2 \frac{c_2 V_{T,k+1}}{h^2} \Delta t_k}\end{aligned}\quad (2.2)$$

where the smoothing coefficient θ is a numerical quantity (Sec.3), c_{ref} (m/s) is the sound speed, ω (m^3) is the particle volume, W (m^{-3}) is the SPH kernel function, h (m) is the kernel support size, c_1 and c_2 are derived from stability analysis (Sec.3).

The application of the SPH filters and of a peculiar version of the forward-backward Euler's scheme, stabilized by the shell SPH filter (Sec.3), to the RANS Balance Equation for the mean Turbulent Kinetic Energy (TKE-BE) provides the following PDE scheme:

$$\begin{aligned}\frac{-}{q_{0,k+1}} &= \frac{\bar{q}_{0,k} + \left(\left\langle P_q \right\rangle_{SH^*,C1,0,k} + \left\langle D_q \right\rangle_{SH^*,C0,0,k} \right) \Delta t_k}{\left(1 + \frac{\bar{\varepsilon}_{0,k}}{q_{0,k}} \Delta t \right)}, \\ \left\langle D_q \right\rangle_{SH^*,C0,0} &= \left\langle \nabla \cdot \left[(\nu_T + \bar{\nu})(\nabla \bar{q}) \right] \right\rangle_{SH^*,C0,0}, \quad \left\langle P_q \right\rangle_{SH^*,C0,0} = 4\nu_{T,0,SHq} \sqrt{(-\left\langle S_m \right\rangle_{C1,0}) \left\langle R_m \right\rangle_{C1,0}}\end{aligned}\quad (2.3)$$

$\left\langle P_q \right\rangle$ (m^2/s^3), $\left\langle D_q \right\rangle$ (m^2/s^3) and $\bar{\varepsilon}$ (m^2/s^3) are the production, diffusion and dissipation rates of the mean TKE. S_m (s^{-2}) and R_m (s^{-2}) are the quadratic invariants of the mean strain-rate tensor and of the mean rotation tensor. The subscript “ SH^* ” indicates that, in the formulation of ν_T, \bar{q} is replaced by its shell SPH filter, i.e., the SPH filter net of the contribution of the computational node.

The application of the SPH filters and the forward-backward Euler's scheme (version of Leroy et al., 2014, [20]) to the BE of the mean-TKE dissipation rate (eps-BE) provides the following PDE scheme:

$$\frac{-}{\varepsilon_{0,k+1}} = \frac{\bar{\varepsilon}_{0,k} + \left(\left\langle P_\varepsilon \right\rangle_{C1,0,k} + \left\langle D_\varepsilon \right\rangle_{C0,0,k} \right) \Delta t_k}{\left(1 + C_{\varepsilon_2} \frac{\bar{\varepsilon}_{0,k}}{q_{0,k}} \Delta t \right)},\quad (2.4)$$

$$\left\langle D_\varepsilon \right\rangle_{C0,0} = \left\langle \nabla \cdot \left[\left(\frac{\nu_T}{\sigma_\varepsilon} + \bar{\nu} \right) (\nabla \bar{\varepsilon}) \right] \right\rangle_{C0,0}, \quad \left\langle P_\varepsilon \right\rangle_{C0,0} = 4C_\mu C_{\varepsilon_1} \bar{q}_0 \sqrt{(-\left\langle S_m \right\rangle_{C1,0}) \left\langle R_m \right\rangle_{C1,0}}$$

where $\left\langle P_\varepsilon \right\rangle$ (m^2/s^4) and $\left\langle D_\varepsilon \right\rangle$ (m^2/s^4) are the SPH eps-BE production and dissipation terms. The constants $(C_\mu, \sigma_\varepsilon, C_{\varepsilon_1}, C_{\varepsilon_2})$ are defined by Launder & Spalding (1974, [33]).

The application of the SPH filters and a peculiar version of the forward-backward Euler's scheme to the BE for the mean concentration \bar{C} (kg/m^3) of a passive pollutant provides the following scheme:

$$\bar{C}_{0,k+1} = \bar{C}_{0,k} + \left\langle \nabla \cdot \left[\left(D_M + \frac{\nu_{T,k+1}}{Sc_T} \right) \nabla \bar{C}_k \right] \right\rangle_{C0,0} \Delta t_k\quad (2.5)$$

where D_M (m^2/s) is the coefficient of molecular diffusion and Sc_T is the turbulent Schmidt number. Eight convergence criteria are built on the non-redundant time-dependent stability conditions and physical-bound conditions of the above PDE schemes (Sec.3).

The SPH Time-Space Ensemble (SPH-TSE) filter combines the SPH (spatial) kernel with an exponential-decaying SPH time kernel of memory-loss factor a_{mem} . The ensemble mean of a generic

quantity A is the weighted sum of the spatial filter over the RANS TKE-averaged eddy size among all the turbulent vortices l_0 (m) and the ensemble mean at the previous time step, at the same point:

$$\bar{A}|_k \approx a_k \langle A \rangle_{l_0,k} + (1-a_k) \bar{A}|_{k-1}, \quad a_k \approx \begin{cases} 1 - e^{-\frac{\min\{\Delta t_k, T_{L,k}\}}{T_{L,k}}}, & T_{L,k} \leq (t_k - t_{IC}) \\ 1 - e^{-\frac{\min\{\Delta t_k, (t_k - t_{IC})\}}{(t_k - t_{IC})}}, & 0 < (t_k - t_{IC}) < T_{L,k} \end{cases} \quad (2.6)$$

where T_L (s) is the Lagrangian integral time scale of turbulence, expressed as function of the peak value of the compensated velocity Lagrangian structure function. Under RANS-SPH simulations, the SPH-TSE filter corrects the ensemble statistics during the post-processing stage of the code algorithm and acts as a convergence criterion to stationary conditions. Under ILES-SPH simulations, the SPH-TSE filter is also used to convert the output LES-filtered quantities into Reynolds' ensemble statistics and to assess the higher-order ensemble moments, the ensemble probability density function and the ensemble cumulative density function. The ensemble statistics for Solid Dynamics are computed via SPH time filter. In other turbulence approaches, the SPH-TSE filter might be straightforwardly adopted to convert the output instantaneous-like quantities into Reynolds' ensemble statistics. The SPH filter applies to all the derivatives in the Balance Equations, and to the functions needing filtering. The SPH filters of a generic function (C_1 -consistent), gradient (C_1 -consistent) and "quasi-Laplacian" (i.e., the divergence of the product of the function gradient by a scalar g) consider contributions from fluid particles " b ", solid particles " s " (of fixed and mobile solid bodies) and fixed-wall elements " w " in the SPH neighbourhood of the computational particle. The SPH filter of the gradient of a generic function f is represented by a C_1 -consistent SPH quadrature formula:

$$\begin{aligned} \langle \nabla f \rangle_{C1,0} = & \sum_b (f_b - f_0) \underline{\underline{B}}_0 \nabla W_b \omega_b + \sum_s (f_{0s} - f_0) \underline{\underline{B}}_0 \nabla W_s \omega_s + \\ & + \underline{\underline{B}}_0 \sum_w (f_{0w} - f_0) \underline{\underline{T}}_w G_{c,0w} + \underline{\underline{B}}_0 \sum_w \left\{ \underline{\underline{T}}_w \left\{ G_{\underline{\underline{l}},0w} \left[\underline{\underline{T}}_w^T (\nabla f)_{0w} \right] \right\} \right\} \end{aligned} \quad (2.7)$$

where $\underline{\underline{B}}$ is the renormalization matrix and $\underline{\underline{T}}$ is the matrix of the directional cosines of the fixed-wall element. The SPH filter of the quasi-Laplacian of f is a C_0 -consistent SPH quadrature formula:

$$\begin{aligned} \langle \nabla \cdot [g \nabla f] \rangle_{C0,0} = & -2g_0 \sum_{b \neq 0} \frac{2\bar{\rho}_b g_b}{\rho_0 g_0 + \rho_b g_b} \frac{(f_b - f_0)}{r_{0b}} \frac{\partial W}{\partial r} \Big|_b \omega_b + \\ & -2g_0 \sum_s \frac{(f_{0s} - f_0)}{r_{0s}} \frac{\partial W}{\partial r} \Big|_s \omega_s - 2g_0 \sum_w (f_{0w} - f_0) L_{c,0w} \end{aligned} \quad (2.8)$$

where r (m) is the distance from the computational particle. The mathematical expression of the fluid-fluid interaction term in (2.8) was formulated in Di Monaco et al. (2011, [34]). Specific C_1 -consistent quadrature formulae apply to positioning-grid points and monitoring points. A kernel-based anti-cluster strategy is used for fluid-fluid and fluid-body interactions. A unified anti-cluster and anti-penetration strategy applies to fluid-wall interactions, based on reactions as numerical collisions.

A long series of spatial reconstruction schemes applies, included RANS SPH Wall Functions (Sec.4). Under fluid flows confined by solid rigid boundaries, the conservative Balance Equation for the particle Control Volume (CV-BE) can be activated to exactly conserve the fluid global volume, net of the frozen-volume regions. CV-BE time integration is ruled by a simple forward-backward Euler's scheme with a post-correction, which determines the following expression:

$$\omega_{k+1} = \omega_{PRE} \left(1 - \frac{\Delta V_{nf,PRE} \omega_{PRE,mcnf}}{V_{PRE,mcnf} \omega_{PRE}} \right), \quad \omega_{PRE} = \frac{m}{\rho_{PRE}} \quad (2.9)$$

V (m³) and ΔV (m³) are the fluid global volume and its error, m (kg) is the particle mass, the subscript " nf " refers to a "non-frozen" volume and " $mcnf$ " stands for "mobile and completely non-frozen".

$\underline{G}_{c,0w}(\text{m}^{-1})$, $\underline{\underline{G}}_{l,0w}$ and $L_{c,0w}(\text{m}^{-2})$ in (2.7)-(2.8) are geometrical quadrature formulae over a single fixed-wall element. The main parts of those source lines of the current code dealing with $\underline{G}_{c,0w}$, $\underline{\underline{G}}_{l,0w}$ and $L_{c,0w}$ are imported from the code SPHERA v.10.0.0 (RSE SpA, 2022, [35]) and were presented in Di Monaco et al. (2011, [34]). Newton-Euler Equations rule Computational Solid Dynamics (CSD): it is the Balance Equation for the Linear Momentum and the Balance Equation for the Angular Momentum. The main parts of those source lines of the current code dealing with the two CSD BEs are imported from the code SPHERA v.10.0.0 (RSE SpA, 2022, [35]) and were presented in Amicarelli et al. (2015, [36]; 2021, [37]; 2022, [38]). The solid-body quantities are instantaneous and interact with the fluid mean variables. Ensemble averaging applies to solid bodies at post-processing.

3. LAGRANGIAN RANS SPH: TIME INTEGRATION AND CRITERIA FOR STABILITY, PHYSICAL BOUNDS AND CONVERGENCE

Within the scope of stability analyses, a Lagrangian PDE can be formally treated as an Ordinary Differential Equation (ODE). A full stability analysis of a Balance Equation involves the propagation of the errors affecting the following quantities: the unknown variable of the current BE of the on-going computational node; the other variables of the current BE of the same node; the unknown variable of the current BE of the other nodes in the computational stencil of the on-going node; the other variables of the current BE of the other nodes in the stencil; the boundary terms of any involved BE of any node. Despite any reasonable simplification, a full stability analysis of the SPH BEs is too much complex in this scope. Thus, systematic stability analyses only consider the errors on the unknown variable of the current BE of the on-going particle. Such kind of analysis is here cited as “direct” stability analysis, for sake of simplicity. The other instability sources are considered under “indirect” stability analyses. They are very simplified and afforded only upon numerical evidence. The computational stencil at boundaries mimic the stencil in the inner domain in terms of quadrature formulae: this is a further motivation to exclude explicit boundary terms from direct stability analyses. These focus only on the propagation of a generic initial error on the ODE unknown variable. This also has to lie within the range of permitted physical values. Thus, specific physical-bound analyses are executed to make the time schemes satisfy this requirement. The numerical constraints obtained from the stability and physical-bound analyses of Sec.3.1-3.7 are 3 Δt -independent stability criteria, 9 Δt -dependent stability criteria and 3 Δt -dependent physical-bound criteria. They are presented in dedicated sections as 13 out of 15 criteria represent original formulations.

The 8 convergence criteria of the code (Sec.3.8) satisfy the Δt -dependent stability and physical-bound criteria and optimize the balance between time truncation errors and elapsed time.

Some of the stability conditions are based on peculiar stability analyses for several blends of forward-backward Euler's time schemes with/without filters, under two test problems. i.e., linear or quadratic-hyperbolic rate of change (Sec.3.2.2-3.2.3, 3.3.3, 3.4.3). Their scope involves any numerical method. Although semi-implicit Euler's scheme and the SPH filter of the quasi-Laplacian held conservation properties, SPH RANS-ME does not strictly conserve momentum. This choice is due to the following motivations: the adoption of a more accurate C_1 -consistent SPH non-conservative filter than a C_0 -consistent SPH conservative filter for the gradients; the reduction of the errors introduced by the ME stabilization term with a non-conservative limiter; the lack of quantification of the velocity-mass covariance term in the mean momentum. The mean fluid mass is exactly conserved at the single-particle level. The mean pollutant mass is strictly conserved at every pair-particle sub-system. The quantification of the SPH time truncation errors on energy conservation is not treated: this topic is deeply addressed by Cercos-Pita et al. (2023, [39]).

3.1. Stability analysis of the RANS SPH Momentum Equation

The direct stability analysis of SPH RANS-ME (2.1) involves the SPH filter of the diffusion term $\langle D_u \rangle$ as an application of (2.8). Considering its inner sub-term and the following assumptions:

$$\bar{\rho}_b \approx \bar{\rho}_0, \quad \bar{v}_0 \approx \bar{v}_b, \quad \bar{v}_{T,0} \approx \bar{v}_{T,b} \quad (3.1)$$

one obtains an ODE under linear rate of change as test problem. The application of Euler's scheme is associated with the following stability domain S_D , where c_2 is approximated as in Sec.3.2.1:

$$S_D = \left(\Delta t \leq \frac{h^2}{c_2 (\bar{v}_{T,0} + \bar{v}_0)} \right), \quad c_2 \equiv -\sum_{b \neq 0} \frac{\omega_b}{r_{0b}} \frac{\partial W}{\partial r} \Big|_b \quad h^2 \geq 0 \quad (3.2)$$

3.2. Stability analysis of the RANS SPH Continuity Equation

A predictor-corrector time scheme applies to SPH RANS-CE (2.2) to enlarge its stability domain: it is the forward-backward Euler's scheme with linear filter (Sec.3.2.1). As a mandatory step for the stability analysis of SPH RANS-CE (Sec.3.2.5), the stability analysis of Euler's scheme with linear filter under linear rate of change (Sec.3.2.4) is derived in Sec.3.2.2, which in turn needs the stability analysis of Euler's scheme with independent filter, under the same test problem (Sec.3.2.3). A peculiar stability condition is obtained for the smoothing coefficient, which rules the corrector stage. This is represented by the SPH partial smoothing of the mean density. It is obtained by the combined application of the SPH partial smoothing of the mean pressure and the Equation of State EoS. Such indirect approach is permitted by the EoS linearity and is preferred to directly smoothing the mean density to reduce the SPH and the machine truncation errors.

3.2.1. Forward-backward Euler's scheme with linear filter applied to the RANS SPH Continuity Equation

A predictor-corrector time scheme applies to SPH RANS-CE (2.2): it is the forward-backward Euler's scheme with linear filter. The predictor stage is a peculiar forward-backward Euler's scheme. The corrector stage is the SPH partial smoothing representing the linear filter (3.12), with θ as smoothing coefficient. Considering the SPH quadrature formulae (2.7)-(2.8), the application of the above-mentioned scheme to (2.2) provides the following expression under a direct stability analysis:

$$\begin{aligned} \bar{\rho}_{0,k+1} &= a_0 \Delta t + b_1 \bar{\rho}_{0,k} + a_1 \bar{\rho}_{0,k} \Delta t, \quad a_1 \equiv [b_1 A + \theta B], \\ b_1 &\equiv 1 - \theta C, \quad A \equiv A_1 + A_2, \quad A_1 \equiv -\left\{ \underline{\underline{B}}_0 \left[\sum_b (\bar{u}_b - \bar{u}_0)_j \nabla W_b \omega_b \right] \right\}_j, \\ A_2 &\equiv 2 \bar{v}_{T,0} \sum_{b \neq 0} \frac{\omega_b}{r_{0b}} \frac{\partial W}{\partial r} \Big|_b, \quad B \equiv -\frac{2}{\sigma_0} \omega_0 \sum_{b \neq 0} \frac{\bar{v}_{T,b}}{r_{0b}} \frac{\partial W}{\partial r} \Big|_b W_b \omega_b, \quad C \equiv \left(1 - \frac{W_0 \omega_0}{\sigma_0} \right) \end{aligned} \quad (3.3)$$

where σ is Shepard's coefficient. The product θC in b_1 is due to the corrector stage and reduces the absolute value of a_1 , thus enlarging the stability domain, especially when A_1 is positive, which is the issue motivating the corrector stage. It occurs under compression conditions, associated with negative divergence of the mean velocity. The diffusion term A_2 is non-positive: it can only enlarge the stability domain. The term θB is collaterally introduced by the corrector stage as a non-negative secondary contribution of the diffusion term and reduces the stability domain. The constant C is equal to 0.855 under cubic beta-spline kernel and $\sigma=1$. Without diffusion, large θ values can set $a_1=0$. With the diffusion term, representing the density/pressure turbulent transport of SPH RANS-CE, $(-A_2 > B \geq 0)$ (Sec.3.2.5) so that the beneficial effect of A_2 is more relevant than the detrimental effect of B and there is no need for large values of θ , which lower accuracy. The scheme (3.3) adopts the following approximations for a feasible assessment of the stability domain (Sec.3.2.2), renouncing to some complicated stability sub-domains for sake of simplicity:

$$A \approx \pm c_1 \frac{c_{ref}}{h} - 2 \frac{c_2 \bar{v}_{T,0}}{h^2}, \quad B \approx 2 \frac{c_2 \bar{v}_{T,0}}{h^2} \frac{W_0 \omega_0}{\sigma_0} \geq 0, \quad c_1 \equiv \max_0 \left\{ \left\{ -\underline{\underline{B}}_0 \left[\sum_b \nabla W_b \omega_b \right] \right\}_j \right\} \frac{h}{c_{ref}} \geq 0 \quad (3.4)$$

The assumption $c_1 \approx c_{1,\max} \approx 0.357$ is based on numerical evidence under stable ILES-SPH simulations. The constant c_2 is approximated by its value computed under a regular spherical distribution of SPH particles, with $h \rightarrow 0$, $h/\Delta x = 1.30$ and using the cubic beta-spline kernel: $c_2 \approx 2.98$. It is worth noticing that the linear filter in (2.2) is consistent because it zeroes in the continuum.

3.2.2. Euler's scheme with linear filter under linear rate of change: stability analysis

The stability analysis of Euler's scheme with linear filter under linear rate of change (Sec.3.2.4) relies on the stability criterion (3.11) for the analogous scheme with independent filter, after assuming the proper definitions of the constants (3.15) and the condition $C_1=C_2=C$, which is satisfied by SPH RANS-CE (Sec.3.2.5). After a long sequence of algebraic passages, Boolean operations, inequality solving, sign analyses, the removal of the most complicated stability sub-domains for sake of simplicity and the definitions of the constants in (3.14), the stability domain reads:

$$S_D \supseteq \left(\theta \geq \frac{A\Delta t}{C(1+A\Delta t)-B\Delta t} \right) \cap \left(\Delta t < \frac{1}{-A+\frac{B}{C}} \right) \cap \left(\Delta t \leq \frac{2-\theta C}{|(1-\theta C)A+\theta B|} \right), \quad B \geq 0 \quad (3.5)$$

3.2.3. Stability analysis of Euler's scheme with independent filter under linear rate of change

Euler's scheme with independent filter is proposed as a predictor corrector scheme for multi-variate ODE under linear rate of change, where Euler's scheme applies as the predictor stage:

$$\frac{dX}{dt} = a_0 + a_1 X, \quad X_{k+1,PRE} = X_k + a_1 X_k \Delta t + a_0 \Delta t \quad (3.6)$$

Under the scope of a direct stability analysis (Sec.3), a_0 and a_1 are constant, whereas X is a generic function. The subscript “ k ” implicitly refers to the time step duration. The possible positivity of a_1 makes (3.6) unstable. Thus, a corrector stage applies as a partial spatial filter:

$$X_{k+1} = (1-\theta) X_{k+1,PRE} + \theta \langle X_{k+1,PRE}(x_b) \rangle_{C-1,IND} \quad (3.7)$$

where the filter $\langle \cdot \rangle_{C-1,indep}$ is any numerical scheme applied to the nodes “ b ” in the computational stencil of the current node “ o ”, provided that the filter is not consistent ($C-1$) to keep its independency “ IND ” from X_{k+1} , but not from $X_{k+1,PRE}$. In case of non-independent filter, a more complicated time scheme applies (Sec.3.2.4). The system (3.6)-(3.7) reads:

$$\begin{aligned} X_{k+1} &= b_1 X_k + a_1^* X_k \Delta t + a_0^* \Delta t + (1-b_1) b_0, \quad a_1^* \equiv a_1 (1-\theta) \\ a_0^* &\equiv a_0 (1-\theta), \quad b_1 \equiv 1-\theta, \quad b_0 \equiv \langle X_{k+1,PRE} \rangle_{C-1,IND} \end{aligned} \quad (3.8)$$

where b_1 is constant and the term with b_0 is non-influential. A simple error analysis permits to express the error E on X at a generic time step “ $k+1$ ” as function of the generic initial error E_0 on X_0 :

$$E_{k+1} = E_0 \left(b_1 + a_1^* \Delta t \right)^{k+1}, \quad \forall k \in \mathbb{N}_0 \quad (3.9)$$

Based on the error analysis above, the stability criterion is introduced:

$$|E_{k+1}| \leq |E_0| \Rightarrow |b_1 + a_1^* \Delta t| \leq 1, \quad \forall k \in \mathbb{N}_0 \quad (3.10)$$

After a sequence of algebraic passages, Boolean operations, inequality solving, sign analyses and adding the constraint ($0 \leq b_1 < 1$) to isolate the only conditions where the present scheme is superior to Euler's scheme, the general stability criterion for the application of Euler's scheme with independent filter under linear rate of change is obtained:

$$\left(a_1^* \leq \frac{1-b_1}{\Delta t} \right) \cap \left\{ \left(a_1^* \geq 0 \right) \cup \left[\left(\Delta t \leq \frac{1+b_1}{|a_1^*|} \right) \cap \left(a_1^* < 0 \right) \right] \right\}, \quad 0 \leq b_1 < 1 \quad (3.11)$$

This is used for the stability analysis of SPH RANS-CE (Sec.3.2.5), where the corrector stage is represented by a peculiar partial smoothing of the mean density.

3.2.4. Euler's scheme with linear filter under linear rate of change

Euler's scheme with linear filter is used by SPH RANS-CE. The associated test problem is the ODE under linear rate of change (3.6). The application of the time scheme above to the cited test problem permits to complete the stability analysis of SPH RANS-CE (Sec.3.2.5).

Euler's scheme with linear filter is presented as a predictor-corrector scheme for multi-variate ODE, where Euler's scheme applies to the predictor stage for the above test problem as in (3.6). The corrector stage is a linear combination of the predictor solution and its spatial filter:

$$X_{k+1} = (1 - \theta) X_{k+1,PRE} + \theta \langle X_{k+1,PRE}(\underline{x}_b) \rangle_{C_0,LIN} \quad (3.12)$$

It is a partial filter where θ is the weighting coefficient of the corrector term and the filter $\langle \cdot \rangle_{C_0,LIN}$ applies to the nodes “ b ” in the computational stencil of the current node “ o ”. The filter is C_0 -consistent, linear in X_k and a linear operator. It applies to the combination of (3.6) and (3.12) as follows:

$$\langle X_{k,b} \rangle_{C_0,LIN} = a_{2,0} + a_{2,1} X_k, \quad \langle a_{1,b} X_{k,b} \rangle_{C_0,LIN} = a_{1,0} + (a_{1,1} + a_{1,2} a_1) X_k, \quad \langle a_{0,b} \rangle_{C_0,LIN} = a_{0,0} + a_{0,1} X_k \quad (3.13)$$

After some algebraic passages, the application of Euler's scheme with linear filter to a multi-variate ODE under linear rate of change provides the following scheme:

$$\begin{aligned} X_{k+1} &= X_k [1 - \theta(1 - a_{2,1})] + X_k \Delta t \{ [1 - \theta(1 - a_{1,2})] a_1 + \theta(a_{1,1} + a_{0,1}) \} + \\ &\quad + \Delta t [a_0 (1 - \theta) + \theta(a_{1,0} + a_{0,0})] + \theta a_{2,0} = \\ &= (1 - \theta C_1) X_k + [(1 - \theta C_2) A + \theta B] X_k \Delta t + D \Delta t + E, \quad A \equiv a_1, \quad B \equiv (a_{1,1} + a_{0,1}), \\ &\quad C_1 \equiv (1 - a_{2,1}), \quad C_2 \equiv (1 - a_{1,2}), \quad D \equiv [a_0 (1 - \theta) + \theta(a_{1,0} + a_{0,0})], \quad E \equiv \theta a_{2,0} \end{aligned} \quad (3.14)$$

where A, B, C_1, C_2, D and E are constants under the hypothesis of a direct stability analysis. The terms in D and E depend on θ and are non-influential in the analysis of Sec.3.2.2. The condition $C_1=C_2$ is assumed in the following as satisfied by SPH RANS-CE (Sec.3.2.5). Eq.(3.14) shows the same form as the analogous scheme with independent filter (3.8), after a proper replacement of the constants:

$$b_1 = (1 - \theta C_1), \quad a_1 = (1 - \theta C_2) A + \theta B, \quad a_0 = D, \quad (1 - b_1) b_0 = E \quad (3.15)$$

3.2.5. Stability analysis of the RANS SPH Continuity Equation

The stability criterion (3.5) of Euler's scheme with linear filter under linear rate of change applies to SPH RANS-CE, considering (3.3)-(3.4), (3.11), (3.15) and $C_1=C_2=C$. After some algebraic passages, Boolean operations, inequality solving, sign analyses, the removal of the most complicated stability sub-domains for sake of simplicity, the omission of redundant conditions and proper choices of worst-case scenarios, the stability criterion for the RANS SPH Continuity Equation is obtained:

$$\begin{aligned} S_D \supseteq & \left[\theta \geq \frac{\left(c_1 \frac{c_{ref}}{h} - 2 \frac{c_2 V_{T,0}}{h^2} \right) \Delta t}{(1 - W_0 \omega_0) \left(1 + c_1 \frac{c_{ref}}{h} \Delta t \right) - 2 \frac{c_2 V_{T,0}}{h^2} \Delta t} \right] \cap \left\{ \Delta t < \frac{1}{\left[c_1 \frac{c_{ref}}{h} + 2 \frac{c_2 V_{T,0}}{h^2 (1 - W_0 \omega_0)} \right]} \right\} \cap \\ & \cap \left[0 < \theta \leq \frac{1}{\left(1 - \frac{W_0 \omega_0}{\sigma_0} \right)} \equiv \theta_{max} \right] \end{aligned} \quad (3.16)$$

3.3. Stability analysis and physical-bound criteria for the RANS Kat&Lau-k-eps SPH Balance Equation of the mean Turbulent Kinetic Energy

A straightforward SPH discretization of TKE-BE returns an ODE with cubic rate of change.

The instability is due to the TKE-production component in the coefficient of the quadratic term. It still determines some complications under a simplified ODE with a quadratic rate of change. Plus, the diffusion component of the quadratic term might provide additional issues. Thus, a peculiar SPH filter, here called “shell SPH filter”, is introduced to obtain an ODE under linear rate of change. This avoids the issues of the quadratic term and permits a simpler and feasible stability analysis for SPH TKE-BE (Sec.3.3.1), without an implicit time scheme. The physical-bound criteria of SPH TKE-BE are derived in Sec.3.3.2. The direct stability analysis of forward-backward Euler’s scheme under linear rate of change (Sec.3.3.3) is mandatory to obtain the stability conditions for SPH TKE-BE.

3.3.1. Stability analysis for the RANS Kat&Lau-k-eps SPH Balance Equation of the mean Turbulent Kinetic Energy

The shell SPH filter is the SPH filter net of the contribution of the computational particle as its own neighbour. This means that the SPH approximations (2.7)-(2.8) are shell SPH filters by construction, but the C₀-consistent SPH filter of a function is replaced by the following filter:

$$\langle f \rangle_{SH,C0,0} = \frac{\sum_{b \neq 0} f_b W_b \omega_b}{\sum_{b \neq 0} f_b \omega_b} = \left(\langle f \rangle_{C0,0} - \frac{f_0 W_0 \omega_0}{\sigma_0} \right) \left(\frac{\sigma_0}{\sigma_0 - W_0 \omega_0} \right) = f_0 \frac{\left(\langle f \rangle_{C0,0} - \frac{W_0 \omega_0}{\sigma_0} \right)}{\left(1 - \frac{W_0 \omega_0}{\sigma_0} \right)} \quad (3.17)$$

where C₀- is preferred to C₁-consistency to obtain a feasible stability analysis. The shell SPH filter is independent from the function at the computational particle f_0 , as clarified by the summations in (3.17). Nonetheless f_0 is fictitiously used for an efficient assessment of this filter as reported in (3.17). The turbulent viscosity is thus replaced by its “TKE-shell” SPH approximation and further assumptions are introduced within the scope of the current stability analysis:

$$\bar{\nu}_{T,0,SHq} \equiv C_\mu \frac{\langle \bar{q} \rangle_{SH,C0,0}^2}{\varepsilon_0}, \quad \bar{\rho}_b \simeq \bar{\rho}_0, \quad \bar{\nu}_b \simeq \bar{\nu}_0, \quad \bar{\nu}_{T,b} \simeq \bar{\nu}_{T,0,SHq} \quad (3.18)$$

The combination of (2.7), (2.8) and (3.18) provides a linear rate of change for SPH TKE-BE, which is formally equal to the test problem in (3.7). The application of a peculiar forward-backward Euler’s scheme (the version of Leroy et al. -2014, [20]- used for their SPH TKE-BE and here stabilized by the shell SPH filter) to the above test problem provides the explicit time scheme (2.3):

$$\bar{q}_{k+1} = \bar{q}_k + a_1 \bar{q}_k \Delta t + a_{0A} \frac{\bar{q}_{k+1}}{\bar{q}_k} \Delta t + a_{0B} \Delta t \Rightarrow \bar{q}_{k+1} = \frac{\bar{q}_k (1 + a_1 \Delta t) + a_{0B} \Delta t}{\left(1 - \frac{a_{0A} \Delta t}{\bar{q}_k} \right)} \quad (3.19)$$

which is formally identical to (3.25). According to the stability analysis of forward-backward Euler’s scheme under linear rate of change (Sec.3.3.3), the stability domain (3.27) applies to (3.19). After algebraic passages and proper overestimations of the error, the stability criterion of SPH TKE-BE is:

$$S_D \supseteq (\Delta t \leq \min \{ \Delta t_1; \Delta t_2 \}), \quad \Delta t_1 \equiv \begin{cases} \frac{1}{D'_1}, & D'_1 > 0 \\ \rightarrow \infty, & D'_1 \leq 0 \end{cases}, \quad \Delta t_2 \equiv \begin{cases} \frac{(\bar{\nu}_{T,0,SHq} + \bar{\nu}_0) \frac{c_2}{h^2}}{D'_2}, & D'_2 > 0 \\ \rightarrow \infty, & D'_2 \leq 0 \end{cases}, \quad (3.20)$$

$$D'_1 \equiv \left(\bar{\nu}_{T,0,SHq} + \bar{\nu}_0 \right) \frac{c_2}{h^2} - \frac{1}{4} \frac{\bar{\varepsilon}_0}{q_k} \left(\frac{\bar{q}_{k+1}}{q_k} + 1 \right),$$

$$D_2' \equiv \frac{\bar{\varepsilon}_0}{q_k} \left[-c_2 \frac{(\bar{V}_{T,0,SHq} + \bar{V}_0)}{h^2} - \frac{1}{2} \frac{\bar{\varepsilon}_0}{q_k} + 2 \sqrt{\left(-\langle S_m \rangle_{C1,0} \right) \langle R_m \rangle_{C1,0}} \frac{\bar{V}_{T,0,SHq}}{q_k} \right]$$

The second/last term of D_2' enlarges the stability domain thanks to forward-backward Euler's scheme. Such benefit is relevant also at very small h , although it vanished for h tending to zero. The constraint on Δt_2 is the counter-part to pay to permit an easier respect of the non-negativity of \bar{q} (Sec.3.3.2).

3.3.2. Physical-bound criteria for the RANS Kat&Lau-k-eps SPH Balance Equation of the mean Turbulent Kinetic Energy

The non-negativity of \bar{q} is imposed in the following demonstration, which relies on the principle of superposition of effects. Considering the sole dissipation term in SPH TKE-BE, one obtains:

$$\bar{q}_{k+1} = \frac{\bar{q}_k}{\left(1 + \frac{\bar{\varepsilon}_k}{q_k} \Delta t \right)} \leq \bar{q}_k, \quad \bar{q}_{k=0} \geq 0 \Rightarrow 0 \leq \bar{q}_{k+1} \leq \bar{q}_k \quad (3.21)$$

The production term cannot reduce \bar{q} by definition. Under the diffusion term only, the non-negativity of \bar{q} requires a further constraint, where the hypothesis on \bar{q}_b is coherent with the worst-case scenario:

$$\bar{q}_{k+1} = \bar{q}_k (1 + a_1 \Delta t) + a_{0B} \Delta t \geq 0, \quad \bar{q}_{k=0} \geq 0, \quad \bar{q}_b = 0 \Rightarrow \Delta t \leq \frac{h^2}{2c_2 (\bar{V}_{T,0,SHq} + \bar{V}_0)} = \Delta t_3 \quad (3.22)$$

The above three cases determine that \bar{q} is always non-negative under forward-backward Euler's scheme provided that (3.22) is satisfied as a lower physical-bound criterion.

Analogously, an upper physical-bound criterion is derived, in case the mean-TKE has to be smaller than a given upper limit \bar{q}_{\max} (m^2/s^2), under specific case-dependent conditions. The demonstration is reduced to the diffusion-only "TKE-BE", i.e., $(P_q \approx \bar{\varepsilon})$. This simplifying hypothesis paves the way to a general result useful for the upper physical-bound criterion of SPH Cm-BE (Sec.3.5), whose time scheme is a degeneration of the scheme for SPH TKE-BE. The upper physical bound is set as follows:

$$\bar{q}_{k+1} = \bar{q}_k (1 + a_1 \Delta t) + a_{0B} \Delta t \leq \bar{q}_{\max}, \quad \bar{q}_b = \bar{q}_{\max} \Rightarrow \Delta t \leq \Delta t_4 = \Delta t_3 \quad (3.23)$$

where the hypothesis on \bar{q}_b is consistent with the worst-case scenario. The upper physical-bound criterion is equal to (3.22) and does not depend on \bar{q}_{\max} . The simple criteria (3.22) and (3.23) are derived under worst-case scenarios, which rarely occur. It is effective to introduce an alternative and more accurate criteria for the lower physical bound:

$$\bar{q}_{k+1} = \bar{q}_k + \left\langle D_q \right\rangle_{SH^*,C0,0} \Delta t \geq 0 \Rightarrow \Delta t \leq \frac{-\bar{q}_k}{\left\langle D_q \right\rangle_{SH^*,C0,0}}, \quad \left\langle D_q \right\rangle_{SH^*,C0,0} < 0 \quad (3.24)$$

The lower physical-bound limiter (3.24) is used for SPH TKE-BE. This does not normally need an upper physical-bound limiter. The simple criteria (3.22) and (3.23), both very constraining for \bar{q} , formally apply to SPH Cm-BE (Sec.3.5). The forward-backward Euler's scheme increases Δt in (3.24) with respect to Euler's scheme, affected by the dissipation term. This is the main motivation for applying forward-backward Euler's scheme to SPH TKE-BE.

3.3.3. Stability analysis of forward-backward Euler's scheme under linear rate of change

The application of forward-backward Euler's scheme, defined in Leroy et al. (2014, [20]) for their SPH TKE-BE, to a generic ODE under linear rate of change provides an explicit time scheme:

$$X_{k+1} = a_1 X_k + a_{0A} \frac{X_{k+1}}{X_k} \Delta t + a_{0B} \Delta t \Rightarrow X_{k+1} = \frac{X_k (1 + a_1 \Delta t) + a_{0B} \Delta t}{\left(1 - \frac{a_{0A} \Delta t}{X_k}\right)}, \quad a_{0A} X \leq 0 \quad (3.25)$$

where the quantities a_1 , a_{0A} and a_{0B} are assumed constants under a direct stability analysis and the hypothesis on the non-negative denominator DEN is satisfied by SPH TKE-BE and SPH Cm-BE. The raw version of the stability criterion (3.10) applies to the result of an error analysis analogous to Sec.3.2.3 and provides the following expression:

$$S_D \equiv (|E_{k+1}| \leq |E_k|) \Leftrightarrow \frac{\left|1 + a_1 \Delta t - \frac{a_{0A} \Delta t}{(X+E)_k} \frac{X_{k+1}}{X_k}\right|}{\left(1 - \frac{a_{0A} \Delta t}{(X+E)_k}\right)} \leq 1, \quad \forall k \quad (3.26)$$

After algebraic passages, Boolean operations, sign and inequality analyses, the removal of redundant conditions and the dismissal of the most complex stability sub-domains for sake of simplicity, the stability domain of this forward-backward Euler's scheme under linear rate of change reads:

$$\begin{aligned} S_D &\supseteq (\Delta t \leq \min \{ \Delta t_1; \Delta t_2 \}) \cap (a_1 \leq 0), \quad \Delta t_1 \equiv \begin{cases} \frac{2}{D_1}, & D_1 > 0 \\ \rightarrow \infty, & D_1 \leq 0 \end{cases}, \quad D_1 \equiv -a_1 + \frac{a_{0A}}{(X+E)_k} \left(\frac{X_{k+1}}{X_k} + 1 \right), \\ \Delta t_2 &\equiv \begin{cases} \frac{-a_1}{D_2}, & D_2 > 0 \\ \rightarrow \infty, & D_2 \leq 0 \end{cases}, \quad D_2 \equiv \frac{-a_{0A}}{X_k (X+E)_k} \left[a_1 (2X_k + E_k) + a_{0A} + a_{0B} \right] \end{aligned} \quad (3.27)$$

where D_2 is always non-influential if ($a_{0B} \leq 0$). After the dismissal of a complicated stability sub-domain, no stable solution is admitted if ($a_1 \leq 0$); it might be necessary a lower limiter to X_k to prevent Δt from diverging. Both cases do not apply to SPH TKE-BE (Sec.3.3.1) or SPH Cm-BE (Sec.3.5). E_k is not responsible for any sign change, as its norm is not expected to be larger than $|X_k|$. The solution for ($a_{0A} X > 0$) does not apply to the current code. Compared to Euler's scheme, the forward-backward Euler's scheme has the advantage to enlarge the stability sub-domain associated with the first Δt constraint and the shortcoming of introducing a second condition depending on D_2 . However, the main advantage of the current scheme is to provide less constraining criteria for the physical bounds of the ODE unknown, at least under some peculiar conditions on the constants (Sec.3.3.1, Sec.3.5).

3.4. Stability analysis and physical-bound criterion for the SPH Balance Equation of the dissipation rate of the mean Turbulent Kinetic Energy

3.4.1. Stability analysis of the SPH Balance Equation for the dissipation rate of the mean Turbulent Kinetic Energy

The direct stability analysis of the RANS SPH Balance Equation for the dissipation rate of the mean TKE (SPH eps-BE) is presented hereafter. The combination of (2.7), (2.8) and (3.1) returns a quadratic-hyperbolic rate of change for SPH eps-BE, formally equal to the test problem of Sec.3.4.3. The application of forward-backward Euler's scheme (the version of Leroy et al., 2014, [20], used for their SPH eps-BE) to (3.28) provides the explicit scheme (2.4), formally identical to (3.32):

$$\frac{d \bar{\varepsilon}}{dt} \Bigg|_{\bar{u}_0} = a_2 \left(\bar{\varepsilon}_0 \right)^2 + a_1 \bar{\varepsilon}_0 + a_0 + \frac{a_{-1}}{\bar{\varepsilon}_0} \Rightarrow \bar{\varepsilon}_{k+1} = \frac{\bar{\varepsilon}_k (1 + a_1 \Delta t) + a_0 \Delta t + \frac{a_{-1} \Delta t}{\bar{\varepsilon}_k}}{\left(1 - a_2 \bar{\varepsilon}_k \Delta t\right)} \quad (3.28)$$

According to the stability analysis of forward-backward Euler's scheme under quadratic-hyperbolic rate of change (Sec.3.4.3), the stability domain (3.34) applies to (3.28). After assigning the proper overestimations to the errors under the worst-case scenarios and assuming coherent and approximated values for the constants (a_0 is non-influential), the stability criterion of SPH eps-BE reads:

$$S_D \supseteq \left(\Delta t \leq \frac{h^2}{c_2 \left(\bar{\nu}_{0,k} + \frac{\bar{\nu}_{T,0,k}}{2\sigma_\varepsilon} \right)} \equiv \Delta t_1, \quad a_2 \equiv -\frac{C_{\varepsilon_2}}{q_{0,k}}, \quad a_1 \approx -\frac{2\bar{\nu}_{0,k}c_2}{h^2}, \quad a_{-1} \approx 2\frac{C_u}{\sigma_\varepsilon} \left(\bar{q}_{0,k} \right)^2 \bar{\varepsilon}_{0,k} \frac{c_2}{h^2} \right) \quad (3.29)$$

3.4.2. Physical-bound criterion for the SPH Balance Equation of the dissipation rate of the mean Turbulent Kinetic Energy

The non-negativity of $\bar{\varepsilon}$ is guaranteed by the current time scheme as demonstrated hereafter via the principle of superposition of effects. Considering the sole dissipation term, $\bar{\varepsilon}$ is always non-negative:

$$\bar{\varepsilon}_{k+1} = \frac{\bar{\varepsilon}_k}{1 + C_{\varepsilon_2} \frac{\bar{\varepsilon}_k}{q_k} \Delta t} \leq \bar{\varepsilon}_k, \quad \bar{\varepsilon}_{k=0} \geq 0 \Rightarrow 0 \leq \bar{\varepsilon}_{k+1} \leq \bar{\varepsilon}_k \quad (3.30)$$

whereas the production term cannot reduce $\bar{\varepsilon}$ by definition. Under the diffusion term only, the non-negativity of $\bar{\varepsilon}$ requires a further constraint:

$$\bar{\varepsilon}_{k+1} = \bar{\varepsilon}_k \left(1 + a_1 \Delta t \right) + a_0 \Delta t + \frac{a_{-1} \Delta t}{\bar{\varepsilon}_k} \geq 0, \quad \bar{\varepsilon}_b = 0 \Rightarrow \Delta t \leq \frac{h^2}{2c_2 \left(\bar{\nu}_0 + \frac{\bar{\nu}_{T,0,k}}{\sigma_\varepsilon} \right)} \equiv \Delta t_2 \quad (3.31)$$

where the hypothesis on $\bar{\varepsilon}_b$ is coherent with the worst-case scenario. The application of the principle of superposition of effects to the above three cases determines that $\bar{\varepsilon}$ is always non-negative under forward-backward Euler's scheme provided that (3.31) is satisfied as a physical-bound criterion. This is more constraining than the stability criterion (3.29). With respect to Euler's scheme, forward-backward Euler's scheme increases the time step duration (3.31) and is thus chosen for SPH eps-BE.

3.4.3. Stability analysis of forward-backward Euler's scheme under quadratic-hyperbolic rate of change

A generic ODE under quadratic-hyperbolic rate of change is the test problem of this stability analysis, where X is here the unknown generic function. The application of forward-backward Euler's scheme (the version of Leroy et al., 2014, [20], used for their SPH eps-BE) to the above test problem reads:

$$X_{k+1} = X_k + a_0 \Delta t + a_1 X_k \Delta t + a_2 X_k X_{k+1} \Delta t + \frac{a_{-1} \Delta t}{X_k} \Rightarrow X_{k+1} = \frac{X_k \left(1 + a_1 \Delta t \right) + a_0 \Delta t + \frac{a_{-1} \Delta t}{X_k}}{\left(1 - a_2 X_k \right)} \quad (3.32)$$

where the functions a_0 , a_1 , a_2 and a_{-1} are assumed as constants under the hypothesis of a direct stability analysis. With respect to Euler's scheme, the quadratic term has here a dependency on X_{k+1} .

The raw version of the stability criterion (3.10) applies to the result of an error analysis analogous to Sec.3.2.3, considering two generic consecutive time steps, a proper application of Cauchy-Schwarz inequality, a constraint on the sign of $a_2 X$ and bounding the magnitude of the initial error:

$$|E_{k+1}| \leq |E_k| \Leftrightarrow \frac{\left| 1 + \Delta t \left(a_1 + a_2 X_{k+1} - \frac{a_{-1}}{(X_k + E_k) X_k} \right) \right|}{\left[1 - a_2 \Delta t (X_k + E_k) \right]} \leq 1, a_2 X \leq 0, |E_0| \leq O \left(\max_k \{ X_k \} \right), \forall k \quad (3.33)$$

After algebraic passages, Boolean operations, sign and inequality analyses, the removal of redundant conditions and the dismissal of the complex stability sub-domains for sake of simplicity, the stability domain of forward-backward Euler's scheme under quadratic-hyperbolic rate of change reads:

$$S_D \supseteq \left[\left(\Delta t \leq \frac{2}{DEN'} \right) \cap (DEN' > 0) \right] \cup (DEN' \leq 0), \quad (3.34)$$

$$DEN' \equiv -a_2(X_{k+1} - X_k - E_k) - a_1 + \frac{a_{-1}}{(X_k + E_k)X_k}, \quad a_2 X \leq 0, \quad a_1 \leq 0, \quad a_{-1} \geq 0, \quad |E_k| \leq X_k$$

3.5. Stability analysis and physical-bound criteria for the RANS SPH Balance Equation of the mean concentration

The forward-backward Euler's scheme applied to SPH Cm-BE (2.5) is the same time scheme of the predictor stage of SPH RANS-CE (Sec.3.2.1). The stability and physical-bound criteria for SPH Cm-BE virtually derived following the stability analysis for SPH RANS-CE would provide too rigid constraints, which are useless to SPH Cm-BE. Instead, an alternative strategy is carried out. Within the scope of direct stability analyses and physical-bound criteria, the only time references which matter are those of the unknown variable. Thus, even if SPH Cm-BE and SPH TKE-BE use different time schemes, these do not show any effective difference in the stability and physical-bound criteria when applied to the above equations. Following (3.20), (3.22) and (3.23), the stability criterion and the physical-bound criteria of SPH Cm-BE read:

$$\Delta t \leq \Delta t_1 = \frac{h^2}{c_2 \left(\frac{\bar{V}_{T,0}}{Sc_T} + D_M \right)}, \quad \Delta t \leq \Delta t_2 = \frac{h^2}{2c_2 \left(\frac{\bar{V}_{T,0}}{Sc_T} + D_M \right)} \quad (3.35)$$

where the latter guarantees the non-negativity of \bar{C} , respects its physical upper limit and is more constraining than the stability criterion. Further, (3.35) does not require the knowledge of the physical upper limit of \bar{C} , whose assessment might be critical, especially under reactive pollutants.

3.6. Stability condition for the coupling of SPH RANS Continuity Equation with SPH RANS Momentum Equation

The Balance Equations for the propagation of acoustic waves in perfect fluids is here represented by the coupling of SPH RANS-CE and SPH RANS-ME, without viscous terms. The associated indirect stability analysis is here omitted. The resulting stability condition for the propagation of acoustic waves, commonly applied in the SPH literature for barotropic WC flows, is used in (3.38).

3.7. Coupling the SPH RANS Momentum Equation with the SPH Trajectory Equation: system time scheme and indirect stability analysis

Time integration of the system of SPH RANS-ME and SPH Trajectory Equation (SPH-TE), and for the code PDEs on Computational Solid Dynamics, is ruled by the semi-implicit Euler's scheme:

$$\bar{\underline{u}}_{k+1} = \bar{\underline{u}}_k + \frac{d\bar{\underline{u}}}{dt} \Big|_{\bar{\underline{u}}, k} (\Delta t)_k, \quad \bar{x}_{k+1} = \bar{x}_k + \bar{\underline{u}}_{k+1} (\Delta t)_k, \quad \Delta t \leq \frac{\Delta x}{|\bar{\underline{u}}|_{\max}} \equiv \Delta t_1 \quad (3.36)$$

where a stability criterion for the indirect stability analysis of the SPH ME-TE system is a classical constraint to the maximum trajectory length covered during a single time step. This is satisfied by the acoustic stability criterion. A further stability criterion is requested by the fluid-wall reactions " $_{FW}$ " which apply to a depth smaller than Δx , where $d_{FW,\max}$ (m) is the depth of the collision region:

$$\bar{\underline{u}}_{FW} \Delta t \leq d_{FW,\max} \Rightarrow \Delta t \leq \frac{d_{FW,\max}}{|\bar{\underline{u}}_{FW}|} \equiv \Delta t_2, \quad |\bar{\underline{u}}_{FW}| \equiv \max_{0,w} \{ \bar{\underline{u}}_0 \cdot \underline{n}_w \}, \quad d_{0w} \leq d_{FW,\max} \quad (3.37)$$

However, the main indirect instability arising from the system SPH ME-TE is due to the deterioration of the SPH particle distribution with time and is fixed by the peculiar ME stabilization term in (2.1).

3.8. RANS Kat&Lau-k-eps SPH system: stability criteria, physical-bound criteria and convergence criteria

The numerical criteria for the RANS SPH Balance Equations, obtained from the direct and indirect stability and physical-bound analyses of Sec.3.1-3.7, are listed in Table 3.1. They are represented by 3 Δt -independent stability criteria, 9 Δt -dependent stability criteria and 3 Δt -dependent physical-bound criteria. The Δt -dependent convergence criteria are built to implicitly satisfy all the Δt -dependent stability and physical-bound conditions, removing any redundancy:

$$\begin{aligned}
 \Delta t &= \min \left\{ \Delta t_{AW}; \Delta t_{MT,FW}; \Delta t_{CE}; \Delta t_{DDq}; \Delta t_{Pq}; \Delta t_{PBq}; \Delta t_{PB\epsilon}; \Delta t_{PBC} \right\}, F_{\Delta t} \in [0.10, 1.00], C_i = 0.10, \\
 \Delta t_{AW} &\equiv F_{\Delta t} \frac{2h}{c_{ref} + |u|_{max}}, \quad \Delta t_{MT,FW} \leq F_{\Delta t} C_{MT,FW} \frac{d_{FW,max}}{u_{FW}}, \quad \Delta t_{CE} \equiv \frac{F_{\Delta t} C_{CE} h}{\left[c_1 c_{ref} + \frac{2c_2 v_{T,0}}{h(1-W_0\omega_0)} \right]}, \\
 \Delta t_{DDq} &\equiv F_{\Delta t} C_{DDq} \cdot \begin{cases} \frac{1}{D'_1}, & D'_1 > 0 \\ \infty, & D'_1 \leq 0 \end{cases}, \quad D'_1 \equiv (\bar{v}_{T,0,SHq} + \bar{v}_0) \frac{c_2}{h^2} - \frac{1}{2} \frac{\bar{\varepsilon}_0}{q_k}, \quad \Delta t_{PBC} \equiv F_{\Delta t} C_{PBC} \frac{h^2}{2c_2 \left(\frac{v_{T,0}}{Sc_T} + D_M \right)}, \\
 \Delta t_{Pq} &\equiv F_{\Delta t} C_{Pq} \cdot \begin{cases} \left(\bar{v}_{T,0,SHq} + \bar{v}_0 \right) \frac{c_2}{h^2}, & D'_2 > 0 \\ \rightarrow \infty, & D'_2 \leq 0 \end{cases}, \quad D'_2 \equiv \frac{\bar{\varepsilon}_0}{q_k} \left[2 \frac{\sqrt{(-\langle S_m \rangle_{C1,0}) \langle R_m \rangle_{C1,0}} v_{T,0,SHq}}{q_k} + \right. \\ &\quad \left. - \frac{c_2}{h^2} \left(\bar{v}_{T,0,SHq} + \bar{v}_0 \right) - \frac{1}{2} \frac{\bar{\varepsilon}_0}{q_k} \right], \\
 \Delta t_{PBq} &\equiv F_{\Delta t} C_{PBq} \cdot \begin{cases} \frac{-q_k}{\langle D_q \rangle_{SH^*,C0,0}}, & \langle D_q \rangle_{SH^*,C0,0} < 0 \\ \infty, & \langle D_q \rangle_{SH^*,C0,0} \geq 0 \end{cases}, \quad \Delta t_{PB\epsilon} \equiv F_{\Delta t} C_{PB\epsilon} \frac{h^2}{2c_2 \left(\bar{v}_0 + \frac{v_{T,0,k}}{\sigma_\epsilon} \right)}
 \end{aligned} \tag{3.38}$$

These 8 independent convergence criteria Δt are ruled by the stability conditions set by the acoustic waves “ $_{AW}$ ”, the fluid-wall reactions in the system of the Momentum-Trajectory Equations “ $_{MT,FW}$ ”, the SPH RANS-CE terms “ $_{CE}$ ”, the diffusion and dissipation terms of SPH TKE-BE “ $_{DDq}$ ”, the production term of SPH TKE-BE “ Pq ”, the lower physical-bound conditions for SPH TKE-BE “ PBq ” and SPH eps-BE “ $PB\epsilon$ ”, and the physical-bound condition for SPH Cm-BE “ PBC ”.

Considering the convergence coefficients C_i , the lowest input value of the optimization factor $F_{\Delta t,min}=1.00$ is meant to guarantee time convergence and its maximum value $F_{\Delta t,max}=10.00$ barely satisfies all the Δt -dependent stability conditions: intermediate values are chosen to find the optimum solution between accuracy and elapsed time.

	SPH RANS-CE	SPH RANS-ME	SPH TKE-BE	SPH eps-BE	SPH Cm-BE	SPH RANS CE-ME	SPH RANS ME-TE
Δt -indep. stab. criteria	Sm.coeff. θ (3.16)	/	shell SPH filter (3.17)(3.18)	/	/	/	stab.term in (2.1)
Δt -dep. stab. criteria	Δt (3.16)	Δt (3.2)	Δt_1 (3.20) Δt_2 (3.20)	Δt_1 (3.29)	Δt_1 (3.35)	directly in (3.38)	Δt_1 (3.36) Δt_2 (3.37)
Phys.-bound criteria	/	/	Δt_3 (3.24)	Δt_2 (3.31)	Δt_2 (3.35)	/	/

Table 3.1. Numerical criteria for RANS SPH Balance Equations, from physical-bound and stability analyses (Sec.3.1-3.7): Δt -independent stability criteria; Δt -dependent stability criteria; physical-bound criteria.

4. RANS WALL FUNCTIONS

The Wall Functions (WFs) of the code of Sec.2 improve the assessment of the mean-TKE dissipation rate and the slip coefficient, used by the boundary mean velocity, without refining the resolution around walls. The local replacement of $\bar{\varepsilon}$ requires a modification of SPH TKE-BE. The above tasks need the WFs for the mean velocity, the mean-TKE and its dissipation rate. They also require the formulation for the roughness length. Further, the WFs need operative definitions for the depths of the turbulent Boundary Layer δ_{τ} (m) and of its Neutral Surface Boundary Layer δ_{NSBL} (m). The first is provided as an input variable (Amicarelli, 2024, [32]); the latter is computed by the code. The much-approximated formulae of the Neutral Outer (or cOre) Boundary Layer (NOBL) provide the missing low-quality information to close the formulations for δ_{NSBL} and δ_{τ} . Further details are shown hereafter.

The combination of the similarity theory of von Karman for NSBL with the definition of the slip coefficient ϕ_s of each particle-wall interaction “ $_{0w}$ ” provides the following expression:

$$\phi_{s,0w} = \begin{cases} 0.00, & \delta_{NSBL,\bar{u}} < r_{0w} \\ \left[\ln\left(\frac{r_{0w}}{z_0}\right) \right]^{-1}, & \max\left\{z_0 e, 11 \frac{\bar{v}}{u_*}\right\} \leq r_{0w} \leq \delta_{NSBL,\bar{u}}, \quad \bar{u}_{\tau,0} \neq \bar{u}_{\tau,w} \\ 1.00, & \text{otherwise} \end{cases} \quad (4.1)$$

which applies to the boundary contributions of the SPH RANS-ME diffusion term. The cut-off distance $z_0 e$ prevents the slip coefficient from overpassing its physical bound of the unity. The relative mean velocity tangential to the wall is \bar{u}_{τ} (m/s), r (m) represents the distance from the wall, z_0 (m) is the roughness length, $k_v=0.400$ is von Karman constant, u^* (m/s) is the friction velocity at wall.

Nikuradse defined three hydraulic-roughness regimes for the roughness length z_0 :

$$z_0 = \begin{cases} \frac{k_s}{30} = \frac{d_{50}}{10} = \frac{H_{sgr}}{5}, & \text{Re}_* \geq 70 \\ \left[\left(\frac{21}{20} - 1 \right) \frac{(\text{Re}_* - 5)}{(70 - 5)} + 1 \right] \frac{\bar{v}}{9u_*} + \left[\left(1 - \frac{1}{30} \right) \frac{(\text{Re}_* - 5)}{(70 - 5)} + \frac{1}{30} \right] \frac{k_s}{30}, & 5 < \text{Re}_* < 70 \\ \frac{\bar{v}}{9u_*}, & \text{Re}_* \leq 5, \quad \text{Re}_* \equiv \frac{u_* k_s}{\nu} \end{cases} \quad (4.2)$$

the rough-wall regime (first line), with an adaptation from van Rijn (1982, [40]) for the median roughness diameter d_{50} (m, which is twice the sub-grid roughness H_{sgr} , m); the smooth-wall regime (last line); an intermediate regime (second line) without universal behaviour, as documented by Bandyopadhyay (1987, [41]). For the latter, simple interpolative formulae have been mathematically derived as the second line of (4.2). The roughness length is used in (4.1) and needs the friction velocity from (4.3) and the input value of d_{50} or H_{sgr} , used to quantify the hydraulic roughness k_s (m).

The WF for the mean-TKE is formulated by the mixing-length model:

$$u_* \approx u_{*,\bar{q}} = \begin{cases} C_{\mu}^{1/4} \sqrt{\bar{q}}, & 11 \frac{\bar{v}}{u_*} < r \leq \delta_{NSBL,\bar{q}} \\ 0, & 0 < r \leq 11 \frac{\bar{v}}{u_*} \end{cases} \quad (4.3)$$

and is used in (4.1), (4.2) and (4.4). The WF for $\bar{\varepsilon}$ reads:

$$\bar{\varepsilon} = \begin{cases} \frac{u_*^3}{k_v r}, & \frac{11\bar{\nu}}{u_*} < r \leq \delta_{NSBL, \bar{\varepsilon}}, \quad P_q = \bar{\varepsilon} \\ 0, & 0 < r \leq \frac{11\bar{\nu}}{u_*} \end{cases} \quad (4.4)$$

and replaces the value computed by SPH eps-BE. Under multiple neighbouring walls, the $\bar{\varepsilon}$ WF of a particle is determined by its particle-wall interaction with the minimum relative distance. Where $\bar{\varepsilon}$ is replaced by its WF, the SPH TKE-BE of the same particle has to be coherently updated by setting $(P_q = \bar{\varepsilon})$. This is alternative to imposing \bar{q} , which can thus vary depending on the diffusion term of SPH TKE-BE and the particle intrusion from NOBL. This simple adaptation of TKE-BE avoids an incoherent reduction of \bar{q} and is alternative to iterative procedures.

The depth δ_{NSBL} in (4.1), (4.3) and (4.4) depends on the variable considered and discriminate particles to possibly assign free-slip conditions and not apply $\bar{\varepsilon}$ WF. Pope (2000, [42]) defined δ_{NSBL} as the distance from the wall where the assessment of the mean velocity via the NSBL WF provides a limited underestimation of ca.10% with respect to the free-stream velocity at the top of the boundary layer:

$$\delta_{NSBL, \bar{u}} = 0.30\delta_T \quad (4.5)$$

The relative error at $r = \delta_{NSBL, \bar{u}}$ between the NSBL WF and the NOBL profile of the mean velocity is used for the operative definition of δ_{NSBL} in the WFs of \bar{q} and $\bar{\varepsilon}$. NOBL profiles are very approximated. They are only useful to feed those proxy variables which do not need accurate NOBL values, such as δ_{NSBL} . The NOBL profiles of u^* , \bar{u}_τ , \bar{q} and $\bar{\varepsilon}$ refer to (4.7)-(4.9). The relative error of 16%, associated with the mean velocity at $0.30\delta_T$, is assumed as the reference error also for \bar{q} and $\bar{\varepsilon}$ WFs so that:

$$\delta_{NSBL, \bar{q}} = 0.16\delta_T, \quad \delta_{NSBL, \bar{\varepsilon}} = 0.11\delta_T \quad (4.6)$$

Considering the NOBL profile for the velocity covariance (Stull, 1988, [43], “Eq.9.5.2.b”), a much-approximated NOBL profile for the height-dependent friction velocity $u_{*,r}$ (m/s) is reported:

$$u_{*,r,NOBL} \approx u_* \left(1 - \frac{r}{\delta_T}\right)^{\frac{1}{2}}, \quad u_{*,r \approx 0} \approx u_* = u_{*,NSBL}, \quad \bar{q} \Big|_{\delta_T} \approx 0, \quad \delta_{NSBL} < r \leq \delta_T \quad (4.7)$$

Following the NOBL mean-velocity gradient (Stull, 1988, [43]), a simple NOBL profile for \bar{u}_τ reads:

$$\bar{u}_{\tau,NOBL} \approx \frac{u_{*,r}}{k_v} \ln\left(\frac{r}{z_0}\right) \approx \frac{u_*}{k_v} \ln\left(\frac{r}{z_0}\right) \left(1 - \frac{r}{\delta_T}\right)^{\frac{1}{2}} = \bar{u}_{\tau,NSBL} \left(1 - \frac{r}{\delta_T}\right)^{\frac{1}{2}}, \quad \delta_{NSBL} < r \leq 0.4\delta_T \quad (4.8)$$

The combination of (4.7), $(P_q \approx \bar{\varepsilon})$, the k-eps definition of P_q , the formulae for ν_T from the mixing-length and k-eps models provides much-approximated NOBL profiles for \bar{q} and $\bar{\varepsilon}$:

$$\begin{aligned} \bar{q}_{NOBL} &\approx \frac{u_*^2}{\sqrt{C_\mu}} \left(1 - \frac{r}{\delta_T}\right) = \bar{q}_{NSBL} \left(1 - \frac{r}{\delta_T}\right), \quad \delta_{NSBL} < r \leq \delta_T, \\ \bar{\varepsilon}_{NOBL} &\approx \frac{u_*^3}{k_v r} \left(1 - \frac{r}{\delta_T}\right)^{\frac{3}{2}} = \bar{\varepsilon}_{SNBL} \left(1 - \frac{r}{\delta_T}\right)^{\frac{3}{2}}, \quad \delta_{NSBL} < r \leq \delta_T \end{aligned} \quad (4.9)$$

The WF for the slip coefficient applies to all the particles with fixed-wall neighbours, also supporting the anti-penetration strategy at walls, whereas the WF for $\bar{\varepsilon}$ even requires the respect of a visibility criterion. Under stationary 1D flows, (4.1) and (4.4) are constant and uniform: they are better computed based on the optional input value $u_{*,input}$. Under the same conditions, \bar{q} is replaced by an

experimental value where (4.4) is activated. These input options avoid potential inconsistencies between the code WFs and the inlet experimental profiles. Under the above conditions, z_0 is assigned from input too (this is also possible, in general, if the rough-wall regime applies everywhere).

5. VALIDATION UNDER GRID TURBULENCE WITH SURFACE POLLUTANT SOURCE; APPLICATION TO AIR-TREATMENT PROCESSES

The code of Sec.2 is here validated under the grid-turbulence approximation (e.g., Bos, 2020, [44]). This is associated with a full-scale application to air-treatment processes. A mechanical grid is implicitly reproduced at the inlet section under the hypotheses of the active-grid limit (Bos, 2020, [44]). The domain sizes are $L_{dom} \times W_{dom} \times H_{dom} = 34.4M_g \times 1.60M_g \times 3.20M_g$, where $W_{dom}=0$ in the 2D reference simulation and $M_g=0.320\text{m}$ is a grid spacing compatible with the Boundary Conditions. The reference system has origin at the bottom centre of the inlet section and x -axis is aligned with $\bar{u}_{inlet} = (U = 1.; 0.; 0.) \text{ m/s}$. The inlet standard deviation of velocity is $\sigma_{u,i,inlet} = 0.05040\text{m/s}$.

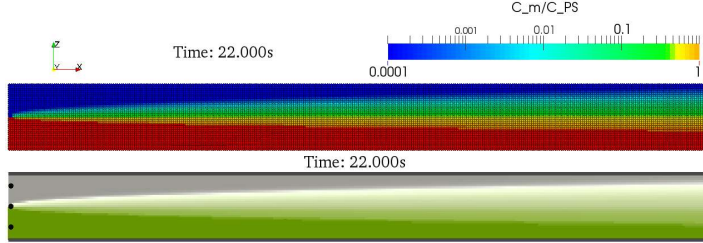


Figure 5.1. Grid turbulence with surface pollutant source: \bar{C} field (vertical slice). Top: non-dimensional field. Bottom: duct (grey and black) airflow past a mechanical grid (black); \bar{C} goes from transparent white to saturated dark green (PS).

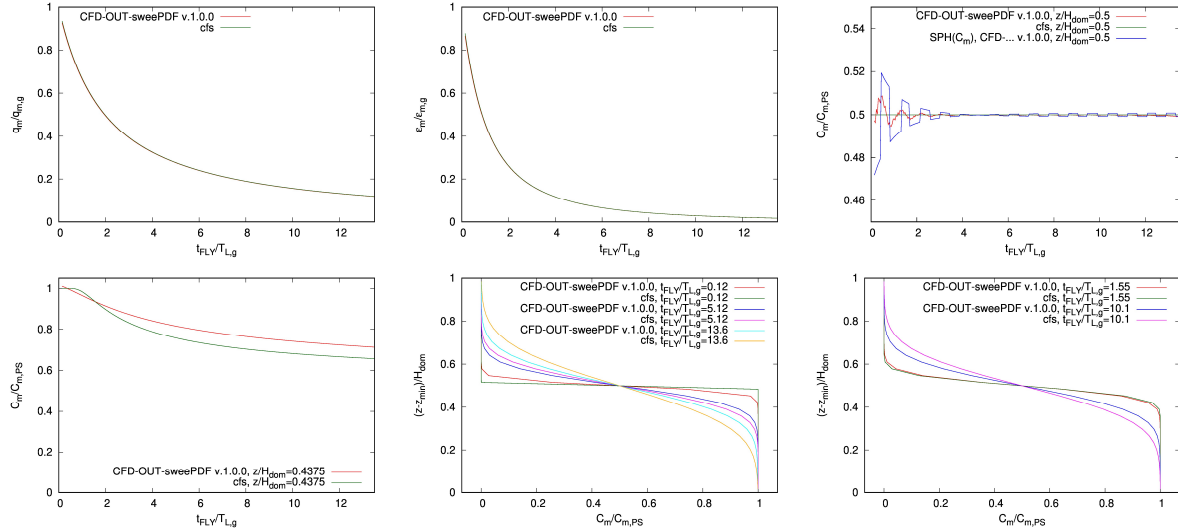


Figure 5.2. Grid turbulence: validations ($t=t_f$). Horizontal profiles of non-dimensional \bar{q} , $\bar{\epsilon}$ and \bar{C} . Vertical profiles of \bar{C} .

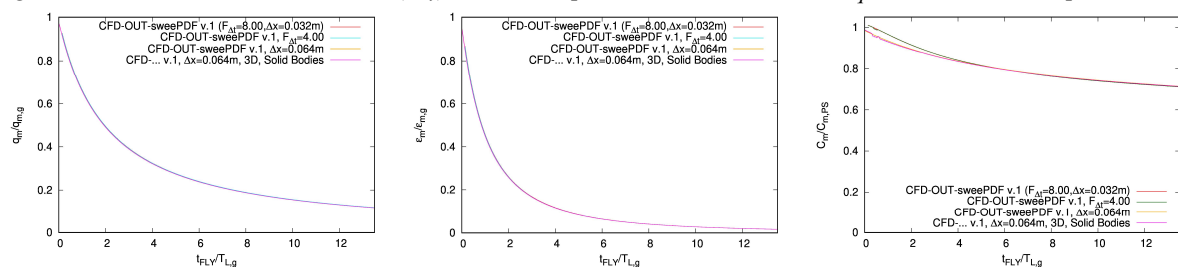


Figure 5.3. Grid turbulence: inter-comparisons for \bar{q} , $\bar{\epsilon}$, \bar{C} . Time/space convergence; 3D validation with solid bodies. The inlet dissipation rate is $\bar{\epsilon}_{inlet} = 2.52 \times 10^{-3} \text{ m}^2/\text{s}^3$. The Pollutant Source (PS) covers the bottom half of the inlet/grid section with mean concentration $\bar{C}_{PS} = 400 \times 10^{-9} \text{ kg/m}^3$. The input value of the coefficient

of molecular diffusion $D_M=1.6\times10^{-5}\text{m}^2/\text{s}$ is representative of NO dispersed in air at $T=25^\circ\text{C}$, being an average between the value of O₂ dispersed in air and ν_{air} , with an input relative error within 9%.

The spatial resolution is defined by the particle size $\Delta x=0.032\text{m}=M_g/10$ and $h/\Delta x=1.30$. The time step duration is ruled by $F_A=8.00$. The optimization of the input background and reference pressure (Amicarelli, 2024, [32]) provides $p_{ref}=1.2\times10^{-2}\text{Pa}$. Top and bottom fixed walls under free-slip conditions reproduce symmetric conditions. The reference simulation is compared with sparring simulations to show convergence in space ($\Delta x=0.064\text{m}$) and time ($F_A=4.00$), and to validate the 3D model adding two solid bodies as symmetric lateral boundaries. Their depth is $3\Delta x$ with body-particle size $\Delta x_s=0.5\Delta x$. The correction to the global fluid volume is activated to zero its errors.

Two lines of stream-wise monitoring points for \bar{q} , $\bar{\varepsilon}$ and \bar{C} are set at $y=0$ and either $z=H_{dom}/2$ or $z=0.4375H_{dom}$. Five vertical lines of monitoring points are set for \bar{C} at $x=0.12, 1.55, 5.12, 10.1, 13.6 t_{FLY}/T_{L,g}$, where $T_{L,g}=0.74\text{s}$ and t_{FLY} (s) is the fly time. This is equal to $(x-x_g)/U$ under Taylor's translation hypothesis on turbulence. The set of closed-form solutions under grid turbulence used for validation combines the formulae reported in Bos (2020, [44]), Anand & Pope (1985, [45]), Sawford (2004, [46]) and Amicarelli (2024, [32]). Non-dimensional variables are obtained via normalization by the following scales: $T_{L,g}, \bar{q}_g, \bar{\varepsilon}_g, \bar{C}_{PS}$ and U_{bulk} (m/s), which is the bulk velocity (i.e., the mean velocity averaged over the inlet section). Stationary conditions are achieved at $t=t_f=22\text{s}$.

The stationary field of \bar{C} propagates downstream as an error function with increasing spread and inhomogeneous dispersion coefficient K_T (Figure 5.1). This test case is set to represent a full-scale application of an air-treatment process, i.e., a duct airflow past a mechanical grid. The bottom flow of NO-polluted air is mixed with the upper flow of clean air to reduce NO levels at the outlet section. The horizontal profiles of the simulated \bar{q} and $\bar{\varepsilon}$ are almost identical to their closed-form solutions, with a hyperbolic behaviour far from grid (Figure 5.2, panels 1-2). The output horizontal profile of \bar{C} along the domain centreline ($z=H_{dom}/2$) is approximately equal to the reference solution, with negligible differences close to the grid, where the default SPH-TSE filter applied to the monitors provides a better performance than the SPH filter (Figure 5.2, panel 3). The profile at $z=0.4375H_{dom}$ shows a general agreement with the reference solution, despite a systematic overestimation of dispersion at $t_{FLY} < T_{L,g}$ and an opposite trend for larger times (Figure 5.2, panel 4). These behaviours are confirmed by the vertical profiles of the simulated \bar{C} , with best performance at $t_{FLY}=1.55T_{L,g}$, and are typical of the state-of-the-art solutions using RANS Balance Equation for \bar{C} along the mean-velocity trajectory, without ad-hoc tuning of Sct (Figure 5.2, panels 5-6). The simulated fields of \bar{q} , $\bar{\varepsilon}$ and \bar{C} converge in time and space, whereas the 3D simulation with solid bodies as lateral boundaries recovers the results of the 2D reference simulation (Figure 5.3).

6. VALIDATION ON EXPERIMENTAL SHEAR FLOW WITH ELEVATED POINT SOURCE; APPLICATION TO OUTDOOR AIR QUALITY WITH STACK RELEASE OF HYDROCARBONS

The code of Sec.2 is here validated under the experimental shear flow of Fackrell & Robins (1982, [47]) with dispersion of a passive scalar emitted by an Elevated Point Source (EPS). The pollutant was a gas mixture of propane and helium. Only the propane was measured, whereas helium kept the experimental mixture neutrally-buoyant close to the source. The test case is associated with an application to Outdoor Air Quality with stack ordinary emission of hydrocarbons (scale ratio 1:1000). The domain sizes are $L_{dom}\times W_{dom}\times H_{dom}=8H_{dom}\times H_{dom}\times H_{dom}$, where $H_{dom}=1.200\text{m}$. The reference system has origin at the bottom centre of the inlet section and x -axis is aligned with the inlet mean velocity. The experimental values of the roughness length $z_0=2.88\times10^{-4}\text{m}$ and the friction velocity at wall $u^*=0.188\text{m/s}$ are provided in input. The mean-TKE inlet profile is related to the experimental vertical profiles of the velocity variances. Following Fackrell & Robins (1982, [47]), the whole $\bar{\varepsilon}$ inlet profile refers to the classical WF for of the Neutral Surface Boundary Layer even beyond its top. For

the inlet conditions, the missing airflow experimental values at $z/\delta_T < 0.05$ are extrapolated via WFs fed by experimental data, with almost-null gradient for \bar{q} to avoid an unphysical trend. Analogously, inlet data at $z/\delta_T > 0.70$ are roughly extrapolated as above, even if they lay out of NSBL. An operative procedure (Amicarelli, 2024, [32]) provides the input value $\delta_T = H_{dom}$.

The experimental Pollutant Source (PS) of propane lies at $x_{PS} = (0, 0, 0.19H_{dom})$, with diameter $D_{PS} = 0.0085\text{m}$. This is small enough not to model jet intrusion. PS mass flow rate $Q_{PS} = 4.71 \times 10^{-7}\text{kg/s}$ (Amicarelli et al., 2011, [48]) is chosen to give a realistic full-scale \bar{C} field under OAQ.

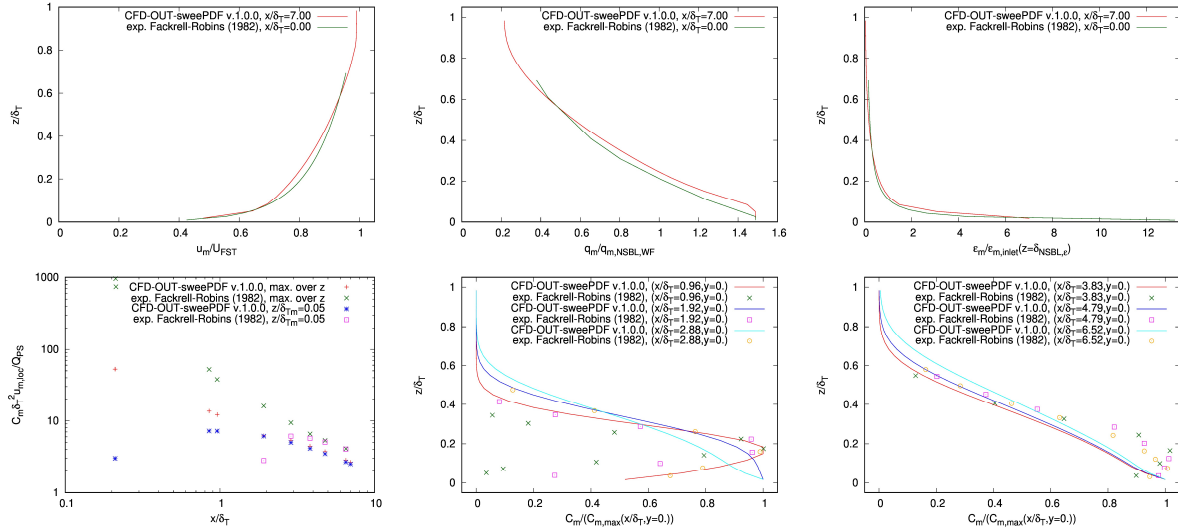


Figure 6.1. Shear flow with EPS: validations for non-dimensional variables ($t=t_f$). Top row: vertical profiles of \bar{u} , \bar{q} , $\bar{\epsilon}$. Bottom row: horizontal and vertical profiles of \bar{C} .

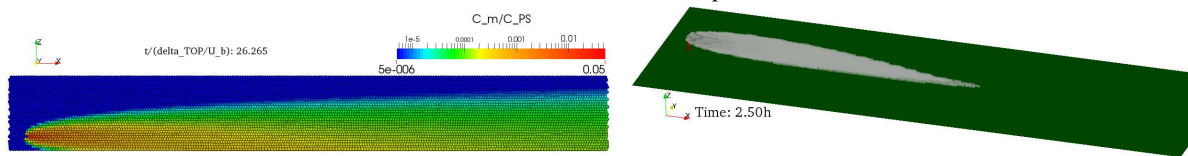


Figure 6.2. Shear flow with EPS: \bar{C} field ($t=t_f$). Left: vertical slice ($y=0$) of the non-dimensional \bar{C} . Right: stack ordinary emission of C_3H_8 (full-scale application) with \bar{C} going from transparent white to saturated black at PS, stack (red) and grassy flat topography (green, covering the whole numerical domain).

It has no experimental reference because it is non-influential in terms of non-dimensional validation. The input value $D_M = 1.41 \times 10^{-5}\text{m}^2/\text{s}$ is returned by a procedure in Amicarelli (2024, [32]) fed by $D_{M,0}(C_3H_8 \text{ in air, } T=0^\circ\text{C}) = 1.2 \times 10^{-5}\text{m}^2/\text{s}$ (Secchi, 2013, [49]).

The spatial resolution is defined by $\Delta x = 0.040\text{m}$ and $h/\Delta x = 1.30$. Optimization procedures provide $F_{\Delta t} = 4.00$ and $p_{ref} = 2.0\text{Pa}$. A top fixed wall under free-slip conditions reproduces symmetric conditions, whereas a fixed wall under WF-driven no-slip conditions represents the bottom wall.

Validation is executed by comparison with the experimental data ($y=0$). A monitoring vertical profile is set at $x/\delta_T = 7.00$ to validate \bar{u} , \bar{q} and $\bar{\epsilon}$. Six vertical profiles are used to validate \bar{C} at $x/\delta_T = 0.96, 1.92, 2.88, 3.83, 4.79, 6.52$, in terms of relative dispersion, via normalization by the maximum value along each vertical. \bar{C} validation is completed by two horizontal profiles. The first extracts the simulated values from the above-mentioned vertical profiles and two additional ones at $x/\delta_T = 0.21, 0.85$. The extracted values are the maxima along each vertical profile. The second horizontal profile represent “ground level” at $x/\delta_T = 0.05$. Normalization of the horizontal profiles considers the local mean velocity at the position of the value extracted (Fackrell & Robins, 1982, [47]). Non-dimensional variables are obtained via division by the following scales: δ_T, \bar{q}_{NSBL} , the free-stream velocity \bar{U}_{FST}

(m/s), $\frac{\bar{Q}_{PS}}{u_{local}\delta_T^2}$ or \bar{C}_{PS} , and $\bar{\varepsilon}_{inlet}(z = \delta_{NSBL,\bar{\varepsilon}})$. Stationary conditions are achieved at $t=t_f=9.0$ s. The

simulated fields of \bar{u} , \bar{q} and $\bar{\varepsilon}$ fairly reproduce the inlet conditions of NBL all over the domain, despite the challenging IC and some inconsistency between WFs and the experimental inlet data, e.g., measurements do not show a null gradient for \bar{q} at ground (Figure 6.1, top panels). The simulated range for the slip coefficient is $\phi_s=0.17-0.21$. The plume shows the typical shape of a diffusion process without velocity autocorrelation, whose role is revised in Fang et al. (2022, [50]). The plume centroid, defined by the set of points featured by \bar{C} maximum along the vertical, lowers with the distance from PS (Figure 6.2, left panel). This is due to the symmetry conditions at ground and the increase in advection with z . The full-scale application associated with the experiment represents an ordinary stack emission of hydrocarbons (C_3H_8) transported over flat grassy topography (Figure 6.2, right panel). The 3D visibility effects gradually highlight the more polluted volumes of air, show the transversal dispersion in both the cross-stream principal directions, and visualize the upstream spread and downstream shrinking of the most polluted portion of the plume. The middle-width horizontal profile of \bar{C} maxima over height roughly follows an exponential decrease with the distance from the source (Figure 6.1, bottom-left panel). The near-ground horizontal profile of \bar{C} shows an upstream growth where the plume centroid approaches the ground and a following decrease under 3D dispersion down to a final convergence to the curve of maxima. The vertical profiles of relative dispersion (Figure 6.1, panels 5-6) describe the transition from an early Gaussian-like shape to an almost-monotone decrease of \bar{C} with z . The simulated profiles show an approximated agreement with the experimental values in the downstream half of the domain, whereas the dispersion mechanism is progressively overestimated when reducing the distance from the source. As $t_{FLY} < ca.T_L$ all over the domain, it is a systematic limit typical of the state-the-art solutions with RANS BEs along the mean-velocity trajectory. This behaviour might also determine some side effects at the lateral boundaries.

7. VALIDATION ON A CONFINED FLOW PAST A WALL-MOUNTED CUBIC OBSTACLE WITH CANYON POLLUTANT SOURCE; IAQ APPLICATION WITH OBSTACLE AND ACCIDENTAL RELEASE OF HYDROCARBONS

The code of Sec.2 is validated under an experimental confined flow past a wall-mounted cubic obstacle (Martinuzzi & Tropea, 1993, [51]) with dispersion of a passive scalar emitted by a Canyon Pollutant Source (CPS). This is set as close as possible to the experimental configuration of Mavroidis et al. (2003, [52]). The test case is associated with an IAQ application, i.e., an accidental release of hydrocarbons from a pipeline in a ventilated indoor parking lot with guard post (scale ratio 1:100). The domain sizes are $L_{dom} \times W_{dom} \times H_{dom} = 15H_b \times 10H_b \times 2H_b$, where $H_b=0.025$ m is the obstacle height. The reference system has origin at the bottom centre of the leading edge of the obstacle and x -axis is aligned with the inlet mean velocity ($x_{inlet}=-4H_b$). The inlet input data on the transporting flow are reconstructed from JFE dataset of Martinuzzi & Tropea (1993, [51]; case labelled as $Re=1.0 \times 10^5$). The experimental profiles at $x=-18H_b$ and x_{inlet} show negligible differences. The average value of the inlet mean-velocity profile is $U_{bulk}=19.81$ m/s. The mean-TKE inlet profile relates to the experimental vertical profiles of the velocity variances. An approximated procedure for the input inlet profile of $\bar{\varepsilon}$ (Amicarelli, 2024, [32]) is fed with the experimental data. The combination of the experimental values for the inlet mean-velocity profile, the roughness length $z_0=1.678 \times 10^{-6}$ m and the friction velocity at wall $u^*=0.899$ m/s (obtained from the velocity covariance) is compatible with a local smooth-wall regime featured by the input sub-grid roughness $H_{sgr}=1.35 \times 10^{-5}$ m. An operative definition for the depth of the turbulent Boundary Layer (Amicarelli, 2024, [32]) provides the input value $\delta_l=0.024$ m, which also implies that $\bar{\varepsilon}$ WF only applies to ca.2/3 of the wall SPH neighbourhood. Non-dimensional variables are obtained via the scales H_b and U_{bulk} . As in Martinuzzi & Tropea (1993, [51]) no scalar was released, the input data on the pollutant refers to the experiment of Mavroidis et al. (2003, [52]). They reproduced a different transporting flow, especially due to the absence of a top

wall, and used another reference system. \bar{C} is expressed in terms of non-dimensional mean concentration under urban canopy $\pi_{\bar{C}}$ (Mavroidis et al., 2003, [52]). The experimental Pollutant Source (PS) lies at $x_{PS}=(-2H_b, 0, 0.5H_b)$, with diameter $D_{PS}=1.044\times 10^{-2}H_b$. This is little enough to avoid modelling any jet intrusion. Q_{PS} and D_M input values are motivated as in Sec.6.

The spatial resolution parameters are $\Delta x=1.5625\times 10^{-3}\text{m}$ and $h/\Delta x=1.30$. Optimization procedures return $F_{\Delta}=4.80$ and $p_{ref}=600\text{Pa}$. Top and bottom fixed walls under WF-driven no-slip conditions represent the channel horizontal walls. Two lateral fixed walls under free-slip conditions impose symmetric conditions to minimize the side effects. Validation of the transporting flow is carried out by comparison with the experimental data for \bar{u} , \bar{v} , \bar{w} and \bar{q} . They are distributed along 14 vertical profiles, 6 of which lie over the obstacle. A sparring simulation is also executed, with k-eps turbulence model replacing the default Kat&Lau-k-eps. The main inter-comparisons consider the results of Atzori et al. (2022, [53]) at $x/H_b=2.00, 3.00$ ($y/H_b=0.00$) for \bar{u} and \bar{q} , obtained with their k- ω , k-eps and R.k-eps models. Their RANS-FVM (Finite Volume Method) spatial multi-resolution is $\Delta x=2.50$, 1.25 , $0.625\times 10^{-3}\text{m}$. Their LES1-FVM model introduce two more nested resolutions $\Delta x=0.312$, $0.156\times 10^{-3}\text{m}$, whereas the LES2-FVM simulation is a more approximated LES at RANS Δx . The number of computational nodes is 6.1×10^6 (RANS-FVM, LES1-FVM) and 12.2×10^6 (LES1-FVM), whereas the current study adopts uniform Δx with 1.3×10^6 nodes. Symmetric experimental profiles are involved in validation so that two measured values are sometimes available at the same position. \bar{C} validation relies on comparisons with the experimental data at two monitoring points. A 2-value average is considered each point (“Table 2” of Mavroidis et al., 2003, [52], sessions “2” and “4”). In the current reference system they are located at $x/H_b=1.50, 4.00$ at ($y/H_b=0.00$, $z/H_b=0.50$).

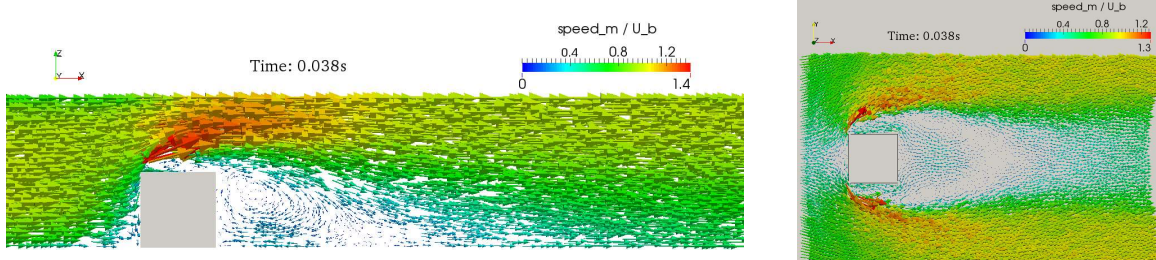


Figure 7.1. Flow past a cube. Localized zooms for \bar{u}/U_b . Vertical ($y/H_b=0$; left) and horizontal ($z=H_b/32$; right) slices.

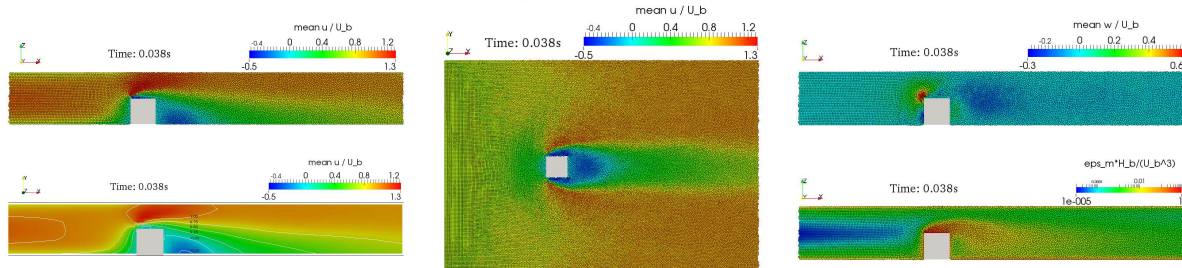


Figure 7.2. Confined flow past a cube. Simulated non-dimensional fields for (from left): \bar{u} (vertical slice, $y/H_b=0$; SPH fluid particles and contours lines from grid points); \bar{u} (horizontal slice, $z=H_b/32$); \bar{w} and $\bar{\epsilon}$ (vertical slices, $y/H_b=0$). Stationary conditions ($t=t_f=0.038\text{s}$) are returned by the criterion based on the SPH-TSE filter (Sec.2). This final time approximately doubles the average fly time of a particle at the outlet section. The cube acts as a bluff body past by the fluid flow setting a further turbulent boundary layer within the channel (Figure 7.1). In the displacement region, i.e., the volume upstream the obstacle where the incoming flow is altered by the obstacle, signs of the upstream recirculation region appear at the toe of the leading face, below the elevated stagnation region. Mean velocity speedups in the upper part of the abrupt shrinkage. The downstream recirculation region, or cavity region, is directly connected to the side recirculation regions, which do not reattach to the obstacle surface (Figure 7.1; Figure 7.2, centre and left). The iso-surface $\bar{u}=U_{bulk}$ shows a vertical cylinder of minima in the upper part of the

displacement region where the flow lifts (Figure 7.6, left). At ground, the iso-surface $\bar{u}=0$, which contains the reversed-flow region, draws a stagnation curve which splits the cavity from the wake region. The length of the cavity at ground is $2.0H_b$. The core of the main vortex within the cavity might represent the head of the arch vortex in Martinuzzi & Tropea (1993, [51]). The peaks of the mean speed (out of scale in Figure 7.1) are recorded around the free edge of the leading face, with \bar{u} and \bar{w} (Figure 7.2, top right) maxima. The asymmetry between the upward flow at the separation zone over the leading face and the downward flow in the upper cavity interest magnitude and spatial cover.

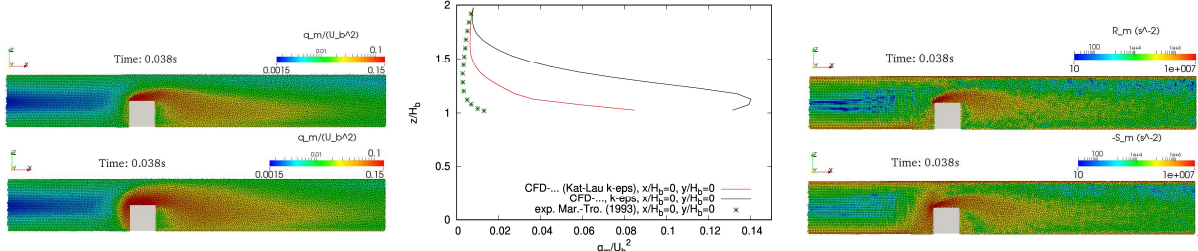


Figure 7.3. Confined flow past a wall-mounted cube. Kat&Lau-k-eps vs. k-eps in CFD-OUT-sweePDF v.1. Left: vertical slices ($y/H_b=0$) of non-dimensional \bar{q} with “Kat&Lau-k-eps” (reference simulation, top) and “k-eps” (sparring simulation, bottom). Centre: validation and inter-comparison for \bar{q} on the monitoring profile over the leading face ($x/H_b=0; y/H_b=0$). Right: vertical slices ($y/H_b=0$) of the simulated fields of R_m and $-S_m$ (ref. sim.).

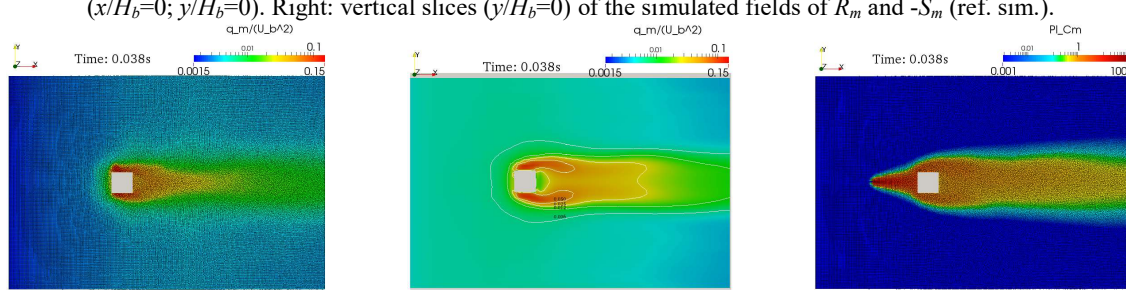


Figure 7.4. Confined flow past a cube with CPS. Non-dimensional fields for (from left to right): \bar{q} (horizontal slice, $z=H_b$; SPH fluid particles); \bar{q} (horizontal slice, $z=H_b/2$; iso-lines from grid points); \bar{C} (horizontal slice, $z=H_b/2$).

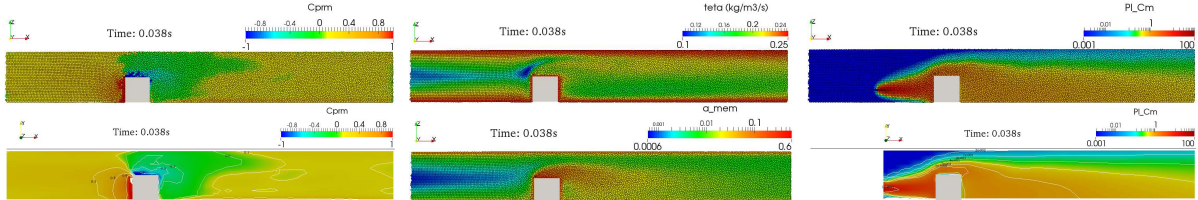


Figure 7.5. Confined flow past a wall-mounted cube with CPS. Vertical slices ($y/H_b=0$) of non-dimensional fields: SPH fluid particles and iso-lines from grid points. From left to right: π_r^- ; θ and a_{mem} ; $\pi_{\bar{C}}$.

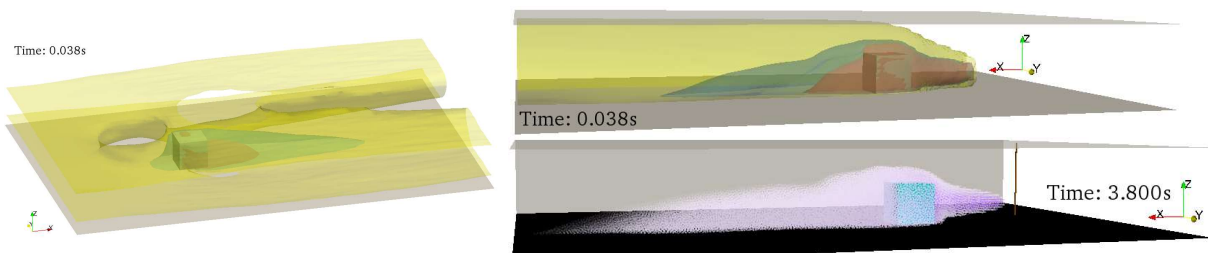


Figure 7.6. Confined flow past a cube with CPS. Iso-surfaces of the non-dimensional mean stream-wise velocity (red: 0.00, cyan: 0.50, yellow: 1.00; left) and $\pi_{\bar{C}}$ (yellow: 0.02, azure: 0.70, red: 1.00; top right). Bottom right: IAQ accidental release of C_3H_8 from a pipe (brown) in a ventilated indoor parking lot with guard post (azure), \bar{C} being shown from transparent white to saturated dark violet at PS.

The mean-TKE peaks $\bar{q} = \text{ca. } 0.15U_b^2$ are recorded on the top and lateral faces of the cube (Figure 7.3, top left; Figure 7.4; left and centre). A zone of local maxima appear in the recirculation region. Near the centre of the trailing face, the mean velocity is more homogeneous with a region of \bar{q} local minima.

The k-eps sparring model of the current code shows a relevant over-production rate of \bar{q} in the displacement region (Figure 7.3, bottom left and centre). The reference “Kat&Lau-k-eps” model is built to reduce this shortcoming of k-eps in the strain-dominated regions, where $-S_m > R_m$ (Figure 7.3, right), still keeping the same performance under shear flows, where $R_m = \text{ca. } -S_m$. The current code benefits from such improvement (Figure 7.3, left and centre). Although \bar{q} were overestimated on the midpoint of the upper edge of the leading face, this error is halved with respect to k-eps.

The spatial pattern of $\bar{\varepsilon}$ (Figure 7.2, bottom right) is similar to \bar{q} , but its range covers five orders of magnitude. The reduced-mean-pressure coefficient varies between $\pi_{p_r}^- = \text{ca. } 1$ in the side recirculation regions and $\pi_{p_r}^- = 1.0$ at the upstream elevated stagnation point (Figure 7.5, left). A depression region is recorded within the abrupt shrinkage over the cube and in the cavity. The smoothing coefficient $\theta = 0.10-0.25$ (Figure 7.5, top centre) minimizes the weight of the corrector stage in SPH RANS-CE (2.2) to enhance accuracy without losing stability, and holds an opposite spatial pattern vs. v_T . The memory-loss factor $a_{mem} = 7.0 \times 10^{-4}-0.56$ (Figure 7.5, bottom centre) quantifies the contribution fraction of the current time step to the SPH-TSE filter and maintains an opposite pattern vs. T_L . The plume spread is abruptly dislocated around the leading and trailing faces of the cube (Figure 7.4, right; Figure 7.5, right). The cavity region is progressively filled with pollutant mass transported from its edges. The range $\pi_{\bar{C}}^- = 0.4-1.0$ features the area downstream the cube in the domain mid-section at $z < \text{ca. } 3/4H_b$. The particle values $\pi_{\bar{C}}^- = 0.02$ interest the top wall since $x = \text{ca. } 5H_b$. The peak of $\pi_{\bar{C}}^-$ along the vertical lowers from the top of the trailing face to the bottom wall, which is reached at $x = \text{ca. } 6H_b$. $\pi_{\bar{C}}^-$ iso-surfaces confirm that the most polluted part of the plume ($\pi_{\bar{C}}^- > 1.00$) is more extended downstream the cube lateral edges than along its centreline (Figure 7.6, top right).

The full-scale application associated with the experiment represents an IAQ accidental release of hydrocarbons from a pipe in a ventilated indoor parking lot with guard post (Figure 7.6, bottom right). The 3D visibility effects gradually highlight the more polluted volumes of air, show the incremental advection and dispersion effects imposed by the presence of the cubic guard post, and visualize the upstream spread and downstream shrinking of the most polluted portion of the plume.

A first validation concerns \bar{u} in the cavity and wake regions (Figure 7.7, left and centre; Figure 7.8). All the RANS models fairly reproduce its values and trends, with limited errors and similar performance. CFD-OUT-sweePDF results lie within the bounds defined by the RANS-FVM state-of-the-art models, although it used a smaller number of nodes by a factor of 5. Its results are close to k- ω -FVM. Both models assess the length of the reversed-flow region in the cavity better than R.k-eps and k-eps, which in turn show larger gradients and superior performance in the upper flow. Near the bottom wall, the current code shows the largest errors among RANS models, but it is the closest to LES results. Its \bar{u} profiles agree with LES-FVM in the reversed-flow region. Its performance seems better than the refined LES1 below the obstacle top in the cavity and is clearly inferior in the wake, with an appreciable delay in the progressive restoration of the undisturbed flow.

CFD-OUT-sweePDF provides the best \bar{q} results in the upper profile, whereas it shows relevant underestimations in the cavity region as well as R.k-eps (Figure 7.7, right). They are both built to reduce the systematic \bar{q} over-prediction of k-eps in the most strain-dominated regions. It is reasonable that if the current code and R.k-eps-FVM provide under-estimations elsewhere in the domain, there k-eps results might appear locally better. k- ω -FVM shows the smallest errors in the cavity, but the worst performance in the upper flow with a profile shape appreciably different from the experiment.

In most of the upper flow, CFD-OUT-sweePDF is close to LES2-FVM, whose data are much more accurate in the cavity region vs. all RANS models, which over-predict the peak height.

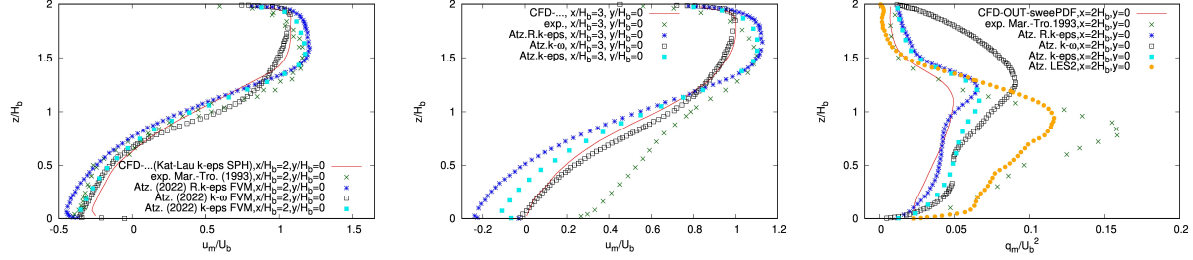


Figure 7.7. Confined flow past a cube ($t=t_f$). Validations and inter-comparisons on \bar{u} (vs. experiment and RANS-FVM at $x/H_b=2,3$) and \bar{q} (vs. experiment, RANS-FVM and LES-FVM; $x/H_b=2$).

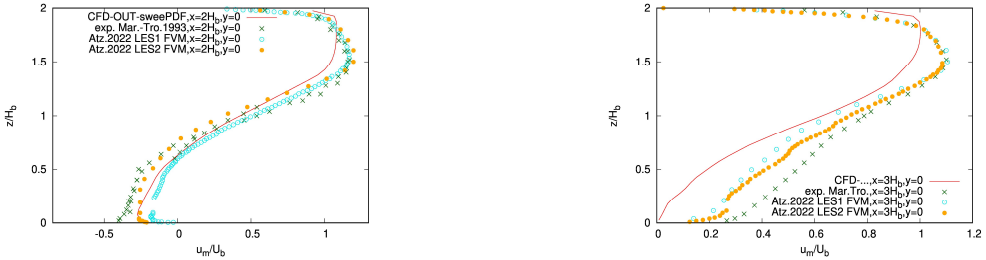


Figure 7.8. Confined flow past a cube ($t=t_f$). Validations (vs. experiment) and inter-comparisons (vs. LES-FVM) on the mean stream-wise velocity at $x/H_b=2,3$.

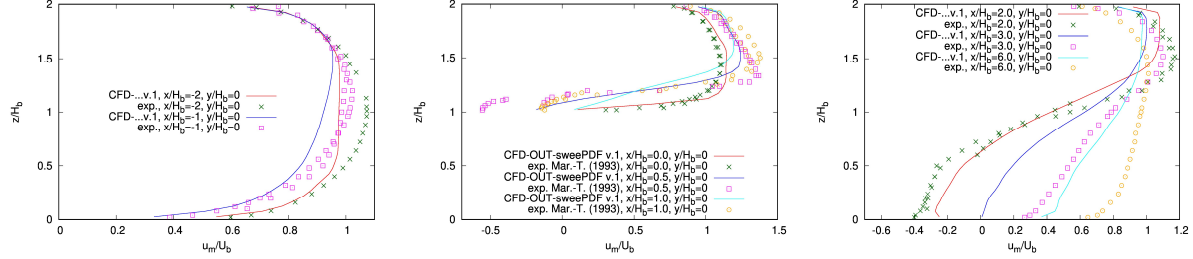


Figure 7.9. Confined flow past a cube. Validations on \bar{u} ($t=t_f$). Monitoring tracks ($y/H_b=0$; from left to right): upstream ($x/H_b=-2,-1$), over ($x/H_b=0,0.5,1$) and downstream ($x/H_b=2,3,6$) the obstacle.

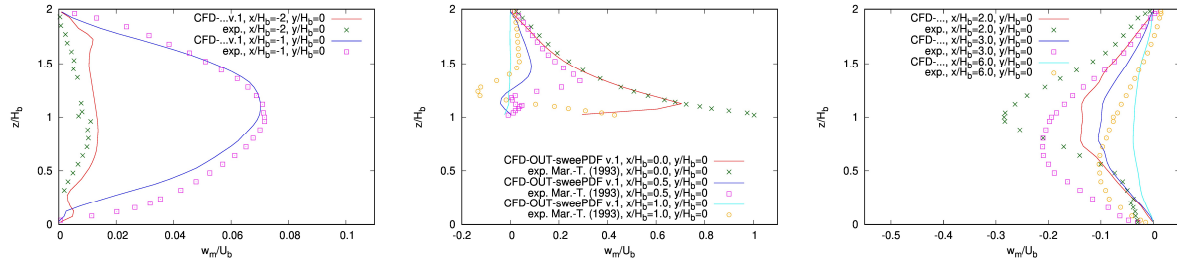


Figure 7.10. Confined flow past a cube. Validations on \bar{w} ($t=t_f$). Monitoring tracks ($y/H_b=0$; from left to right): upstream ($x/H_b=-2,-1$), over ($x/H_b=0,0.5,1$) and downstream ($x/H_b=2,3,6$) the obstacle.

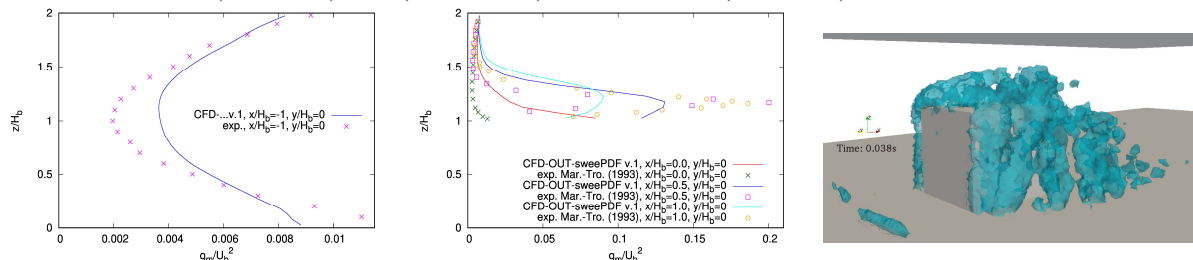


Figure 7.11. Confined flow past a cube. Further validations on \bar{q} ($t=t_f$). Monitoring tracks ($y/H_b=0$) upstream ($x/H_b=-2,-1$; left) and over ($x/H_b=0,0.5,1$; centre) the obstacle. Iso-surfaces at $Q_m=3.0\times 10^5/\text{s}^2$ (right).

When comparing the relative errors on \bar{q} and \bar{u} , one considers that \bar{q} errors in terms of σ_u are much smaller and that these RANS-FVM models are representative of the state of the art. LES2-FVM provides very accurate results even working out of scale, at RANS Δx . Its performance seems slightly better than LES1-FVM, executed at a more proper Δx . These signs highlight the complexity of the current validation, even among the most advanced and recent codes.

Further validations are carried out by comparison with all the available experimental data, where other numerical results seem absent. Some profiles are reported both on the stream-wise and cross-stream monitoring tracks to show the spatial progression along each track. The simulated \bar{u} agrees

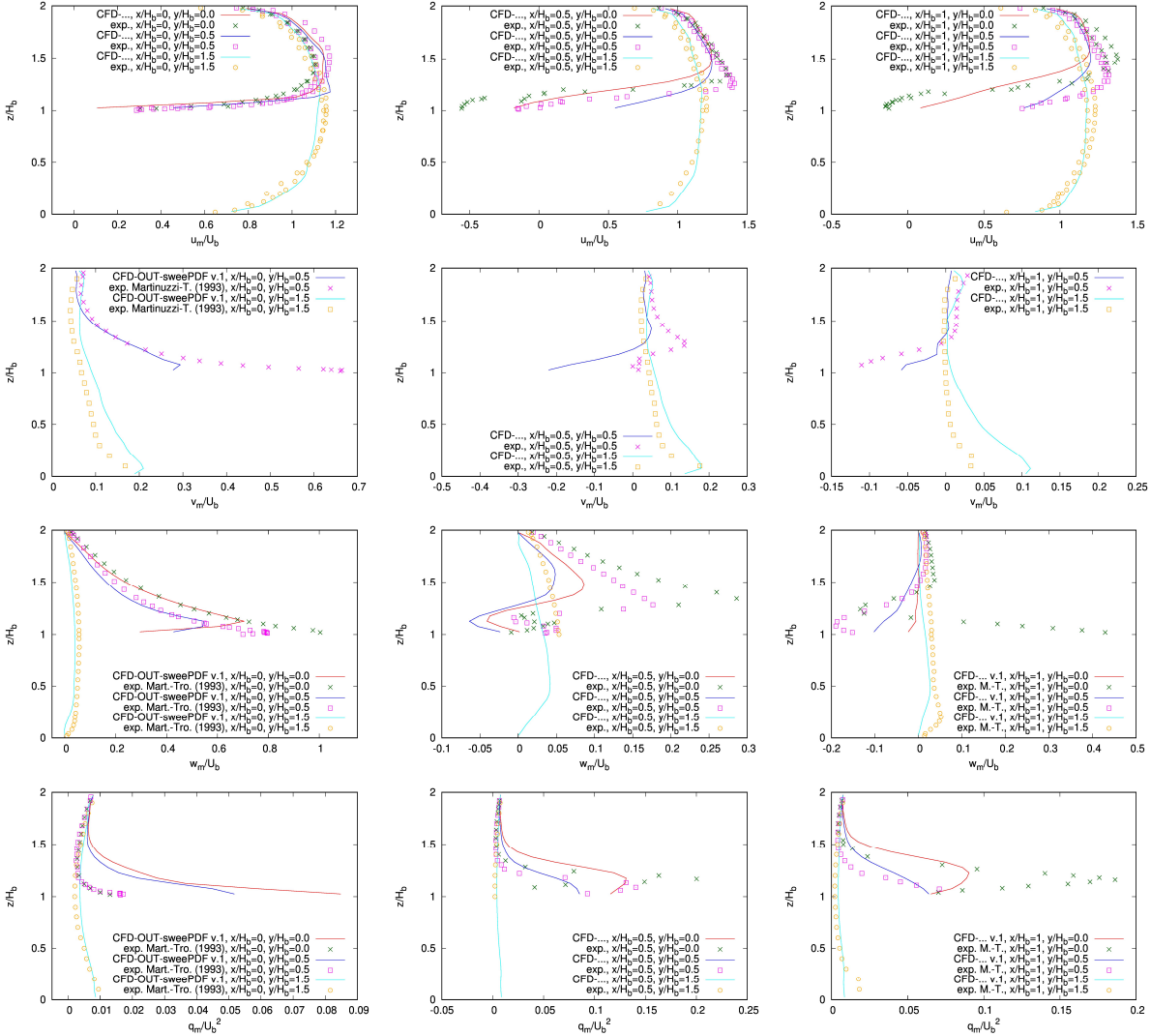


Figure 7.12. Flow past a cube. Validations (lateral tracks; $t=t_f$). Rows (from top): \bar{u} , \bar{v} , \bar{w} , \bar{q} . Columns (from left): tracks ($y/H_b=0, 0.5, 1.5$) crossing the leading face ($x/H_b=0$), the obstacle centre ($x/H_b=0.5$) or the trailing face ($x/H_b=1$).

t/t_f	x/H_b	sim. (ref.)	exp.	sim. (station. criter.)
1.00	1.500	0.831	0.796	0.839
1.00	4.000	0.743	0.276	0.739
0.33	1.500	0.011	/	0.018

Table 7.1. Non-dimensional mean concentration $\pi_{\bar{C}}$ ($y=0, z=0.5H_b, t=t_f$). Validation: simulated (“sim.”) vs. experimental (“exp.”) values. Inter-comparison: SPH-TSE filter (reference monitor post-processing) vs. SPH filter (last column). with measurements, especially in the displacement region, the shrinkage above the obstacle and the cavity (Figure 7.9; Figure 7.12, row 1). The spatial trends are correctly reproduced included the

velocity reduction approaching the top and bottom walls. Nonetheless, the gradients are smoother and an appreciable delay is confirmed in restoring the conditions of undisturbed flow.

The simulated profiles of \bar{v} (Figure 7.12, row 2) and \bar{w} (Figure 7.10; Figure 7.12, row 3) generally show appreciable but limited errors, with spatial trends similar to measurements. Relevant errors affect \bar{v} around the top face of the cube. The simulated gradients of \bar{w} are smoother than the experimental ones and some anomalies in \bar{w} are recorded over the trailing face of the cube. The best performance on \bar{w} regards the uplift of the approaching flow and the entry to the shrinkage region.

Further validations on \bar{q} concern the profiles upstream and over the cube (Figure 7.11, left and centre; Figure 7.12, row 4). Results show spatial trends similar to measurements but smoother gradients. The displacement region is fairly reproduced. The same overestimation of Figure 7.3, already discussed, is shown again on the track. Limited \bar{q} underestimations occur downstream, over the obstacle.

The iso-surfaces $Q_m=3.0\times10^5/s^2$ detect the most “rotation-dominated” coherent turbulent structures of the domain, following the Q -criterion (Jeong & Hussain, 1995, [54]) here applied to the mean-velocity (Figure 7.11, right). Positive/negative values of the quadratic invariant of the mean-velocity gradient tensor $Q_m=R_m+S_m$ (s^{-2}) denote rotation-/strain-dominated volumes. The detected vortices which lie in the lateral and top recirculation regions are described by Martinuzzi & Tropea (1993, [51]). The near-ground structures might belong to the horseshoe vortex reported by the same authors.

The simulated \bar{C} matches the experimental value in the cavity region, whereas the overestimation in the wake region seems motivated by the confinement effect of the top-wall, absent in the scalar experiment (Table 7.1). The systematic bias of the state-of-the-art formulations for K_T might play a secondary role at these monitoring points as $t_{FLY}=O(T_L)$. The negligible difference between the SPH-TSE and the SPH filters of \bar{C} at $t=t_f$ confirms its effective use as a criterion to stationary condition, whereas the earlier relative differences motivate the use of SPH-TSE under non-stationary conditions.

8. CONCLUSIONS

The synthetic conclusions of this study are reported in the abstract. More details follow hereafter. The largest errors of the code are recorded at the obstacle edges for the transporting fluid or refer to the limits of the formulation for the dispersion coefficient. These are typical of the state-of-the-art solutions using RANS Balance Equation for \bar{C} along the mean-velocity trajectory, without tuning SCT . The possible novelties of the current study within the SPH scope are listed hereafter: the adoption of a state-of-the-art 2-equation 1st-order turbulence closure (Kat&Lau-k-eps or R.k-eps); RANS BE for the mean concentration; RANS WC-SPH Continuity Equation (with turbulent transport term); 13 peculiar stability and physical-bound conditions for SPH BEs including SPH shell filter, a ME stabilization term and a RANS-SPH smoothing coefficient; the SPH-TSE filter to compute or preserve the accuracy of ensemble statistics and its difference with SPH filter as a criterion to stationary conditions; the formulation validity at moderate Re and its gradual degeneration into NS (Navier-Stokes) - SPH under laminar flows; the systematic use of C₁-consistent SPH quadrature formulae for gradient and function approximations, also at boundaries; SPH application to air quality. Other possible novelties relate to a wider scope of numerical methods: the application of the SPH-TSE filter to convert LES-filtered or instantaneous-like quantities computed by any method into ensemble statistics; the assessment of the Lagrangian integral time scale as function of the peak value of the compensated velocity Lagrangian structure function in a CFD code (here omitted for sake of brevity); the dependency of WFs on the three hydraulic-roughness regimes and the depths of the NSBL and the turbulent BL; the adaptation of TKE-BE to ε WF; stability conditions for several blends of forward-backward Euler's time schemes with/without filters, under linear or quadratic-hyperbolic rate of change; the application of a Lagrangian CFD method to turbulent flows with pollutant dispersion using a sole set of computational nodes.

Acknowledgements

This study received no public funding. Formal details on the code CFD-OUT-sweePDF are reported at <https://www.researchgate.net/profile/Andrea-Amicarelli> and github.com/AndreaAmicarelli-personal. Videos on the results of CFD-OUT-sweePDF are published at <https://www.youtube.com/@andrea.amicarelli>.

REFERENCES

- [1] J. Monaghan, “Smoothed Particle Hydrodynamics,” *Annu. Rev. Astron. Astrophys.*, vol. 30, pp. 543-74, 1992.
- [2] J. Boris, F. Grinstein, E. Oran and R. Kolbe, “New insights into large eddy simulation,” *Fluid Dynamics Research*, vol. 10, pp. 199-228, 1992.
- [3] R. Vacondio, B. Rogers and P. Stansby, “Accurate particle splitting for smoothed particle hydrodynamics in shallow water with shock capturing,” *Int. J. Numer. Meth. Fluids*, p. DOI: 10.1002/fld.2646, 2011.
- [4] J.-C. Marongiu, F. Leboeuf, J. Caro and E. Parkinson, “Free surface flows simulations in Pelton turbines using an hybrid SPH-ALE method,” *J. Hydraul. Res.*, vol. 47, pp. 40–49, DOI: 10.1080/00221686.2010.9641244, 2010.
- [5] P. Koukouvinis, J. Anagnostopoulos and D. Papantonis, “An improved MUSCL treatment for the SPH-ALE method: comparison with the standard SPH method for the jet impingement case,” *International Journal for Numerical Methods in Fluids*, vol. 71, no. 9, p. 1152–1177. DOI: 10.1002/fld.3706, 2013.
- [6] A. Ferrari, M. Dumbser, E. Toro and A. Armanini, “A new 3D parallel SPH scheme for free surface flows,” *Computers & Fluids*, vol. 38, pp. 1203-1217, doi:10.1016/j.compfluid.2008.11.012, 2009.
- [7] M. Antuono, A. Colagrossi and S. Marrone, “Numerical diffusive terms in weakly-compressible SPH schemes,” *Comput. Phys. Commun.*, vol. 183, pp. 2570-2580, 2012.
- [8] A. Di Mascio, M. Antuono, A. Colagrossi and S. Marrone, “Smoothed particle hydrodynamics method from a large eddy simulation perspective,” *Physics of Fluids*, vol. 29, no. 035102, p. doi: 10.1063/1.4978274, 2017.
- [9] D. Meringolo, Y. Liua, X.-Y. Wang and A. Colagrossi, “Energy balance during generation, propagation and absorption of gravity waves through the d-LES-SPH model,” *Coastal Engineering*, vol. 140, pp. 355–370, <https://doi.org/10.1016/j.coastaleng.2018.07.007>, 2018.
- [10] P. Sun, A. Colagrossi, S. Marrone, M. Antuono and A.-M. Zhang, “A consistent approach to particle shifting in the δ -Plus-SPH model,” *Computer Methods in Applied Mechanics and Engineering*, vol. 348, pp. 912-934, DOI: 10.1016/j.cma.2019.01.045, 2019.
- [11] H. Gotoh and T. Sakai, “Key issues in the particle method for computation of wave breaking,” *Coastal Engineering*, vol. 53, pp. 171-179, doi:10.1016/j.coastaleng.2005.10.007, 2006.
- [12] E. Lo and S. Shao, “Simulation of near-shore solitary wave mechanics by an incompressible SPH method,” *Applied Ocean Research*, vol. 24, pp. 275-286, doi:10.1016/S0141-1187(03)00002-6, 2002.
- [13] B. Ren, H. Wen, P. Dong and Y. Wang, “Numerical simulation of wave interaction with porous structures using an improved smoothed particle hydrodynamic method,” *Coastal Engineering*, vol. 88, pp. 88–100, <http://dx.doi.org/10.1016/j.coastaleng.2014.02.006>, 2014.
- [14] L. Sigalotti, C. Alvarado-Rodríguez, J. Klapp and J. Cela, “Smoothed Particle Hydrodynamics Simulations of Water Flow in a 90° Pipe Bend,” *Water*, vol. 13, no. 1081, p. <https://doi.org/10.3390/w13081081>, 2021.
- [15] D. Isik and Z. He, “SPH Viscous Flow Around a Circular Cylinder: Impact of Viscous Formulation and Background Pressure,” *International Journal of Computational Fluid Dynamics*, vol. 35, no. 6, pp. 451-467, DOI: 10.1080/10618562.2021.1979523, 2021.
- [16] H. Shi and Y. Huang, “A GPU-Based d-Plus-SPH Model for Non-Newtonian Multiphase Flows,” *Water*, vol. 14, pp. 1-21, <https://doi.org/10.3390/w14111734>, 2022.
- [17] M. Okrashevski, N. Buerkle, R. Koch and H.-J. Bauer, “Smoothed particle hydrodynamics physically reconsidered: The relation to explicit large eddy simulation and the issue of particle duality,” *Phys. Fluids*, vol. 34, no. 115108, p. <https://doi.org/10.1063/5.0105104>, 2022.

- [18] D. Violeau and R. Issa, “Numerical modelling of complex turbulent free-surface flows with the SPH method: an overview,” *Int. J. Numer. Meth. Fluids*, vol. 53, pp. 277-304, DOI: 10.1002/fld.1292, 2007.
- [19] M. Ferrand, D. Laurence, B. Rogers, D. Violeau and C. Kassiotis, “Unified semi-analytical wall boundary conditions for inviscid laminar or turbulent flows in the meshless SPH method,” *International Journal for Numerical Methods in Fluids*, vol. 71, no. 4, pp. 446-472, DOI: 10.1002/fld.3666, 2013.
- [20] A. Leroy, D. Violeau, M. Ferrand and C. Kassiotis, “Unified semi-analytical wall boundary conditions applied to 2-D incompressible SPH,” *Journal of Computational Physics*, vol. 261, pp. 106–129, <http://dx.doi.org/10.1016/j.jcp.2013.12.035>, 2014.
- [21] D. De Padova, M. Mossa and S. Sibilla, “SPH Modelling of Hydraulic Jump Oscillations at an Abrupt Drop,” *Water*, vol. 9, no. 790, p. doi:10.3390/w9100790, 2017.
- [22] W. Welton and S. Pope, “PDF model calculations of compressible turbulent flows using Smoothed Particle Hydrodynamics,” *Journal of Computational Physics*, vol. 134, pp. 150-168, 1997.
- [23] T. Canor and V. Denoël, “Transient Fokker-Planck-Kolmogorov equation solved with smoothed particle hydrodynamics method,” *International Journal for Numerical Methods in Engineering*, vol. 94, no. 6, pp. 535-553, DOI: 10.1002/nme.4461, 2013.
- [24] A. Mayrhofer, D. Laurence, B. Rogers and D. Violeau, “DNS and LES of 3-D wall-bounded turbulence using Smoothed Particle Hydrodynamics,” *Computers & Fluids*, vol. 115, pp. 86-97, <https://doi.org/10.1016/j.compfluid.2015.03.029>, 2015.
- [25] G. Efthimiou, S. Andronopoulos, R. Tavares and J. Bartzis, “CFD-RANS prediction of the dispersion of a hazardous airborne material released during a real accident in an industrial environment,” *Journal of Loss Prevention in the Process Industries*, vol. 46, pp. 23-36, <http://dx.doi.org/10.1016/j.jlp.2017.01.015>, 2017.
- [26] D. Thomson, “Criteria for the selection of the stochastic models of particle trajectories in turbulent flows,” *Journal of Fluid Mechanics*, vol. 180, pp. 529-556, 1987.
- [27] D. Haworth, “Progress in probability density function methods for turbulent reacting flows,” *Progress in Energy and Combustion Science*, vol. 36, pp. 168–259, DOI: 10.1016/j.pecs.2009.09.003, 2010.
- [28] S. Pope, “PDF methods for turbulent reacting flows,” *Progress in Energy and Combustion Science*, vol. 11, p. 119–192, 1985.
- [29] J. Meeder and F. Nieuwstadt, “Large-eddy simulation of the turbulent dispersion of a reactive plume from a point source into a neutral atmospheric boundary layer,” *Atmospheric Environment*, vol. 34, pp. 3563-3573, 2000.
- [30] I. Vinkovic, C. Aguirre, M. Ayraut and S. Simoëns, “Large-eddy simulation of the dispersion of solid particles in a turbulent boundary layer,” *Boundary-Layer Meteorol*, vol. 121, pp. 283-311, DOI 10.1007/s10546-006-9072-6, 2006.
- [31] L. Gicquel, P. Givi, F. Jaberi and S. Pope, “Velocity filtered density function for large eddy simulation of turbulent flows,” *PHYSICS OF FLUIDS*, vol. 14, no. 3, pp. 1196-1213, DOI: 10.1063/1.1436496, 2002.
- [32] A. Amicarelli, CFD-OUT-sweePDF v.1.0.0: documentation file, pp.1-133, 2024.
- [33] B. Launder and D. Spalding, “The numerical computation of turbulent flows,” *Comput. Meth. Applied Mech. Eng.*, vol. 3, no. 2, pp. 269-289, 1974.
- [34] A. Di Monaco, S. Manenti, M. Gallati and S. Sibilla, “SPH modeling of solid boundaries through a semi-analytic approach,” *Engineering Applications of Computational Fluid Mechanics*, vol. 5, no. 1, pp. 1-15, DOI: 10.1080/19942060.2011.11015348, 2011.
- [35] SPHERA (RSE SpA), “<https://github.com/GiordanoAgateRSE/SPHERA>,” 2022. [Online].
- [36] A. Amicarelli, R. Albano, D. Mirauda, G. Agate, A. Sole and R. Guandalini, “A Smoothed Particle Hydrodynamics model for 3D solid body transport in free surface flows,” *Computers & Fluids*, vol. 116, p. 205–228; DOI 10.1016/j.compfluid.2015.04.018, 2015.
- [37] A. Amicarelli, S. Manenti and M. Paggi, “SPH modelling of dam-break floods, with damage assessment to electrical substations,” *International Journal of Computational Fluid Dynamics*, vol. 35, no. 1-2, pp. 3-21; DOI 10.1080/10618562.2020.1811240, 2021.

- [38] A. Amicarelli, E. Abbate and A. Frigerio, “SPH modelling of a dike failure with detection of the landslide sliding surface and damage scenarios for an electricity pylon,” *International Journal of Computational Fluid Dynamics*, vol. 36, no. 4, pp. 265-293, DOI 10.1080/10618562.2022.2108020, 2022.
- [39] J. Cercos-Pita, P. Merino-Alonso, J. Calderon-Sanchez and D. Duque, “The role of time integration in energy conservation in Smoothed Particle Hydrodynamics fluid dynamics simulations,” *European Journal of Mechanics - B/Fluids*, vol. 97, pp. 78-92, <https://doi.org/10.1016/j.euromechflu.2022.09.001>, 2023.
- [40] L. Van Rijn, “The prediction of Bed-Forms and Alluvial Roughness, Report,” Delft Hydraulics laboratory, The Netherlands, 1982.
- [41] P. Bandyopadhyay, “Rough-wall turbulent boundary layers in the transition regime,” *Journal of Fluid Mechanics*, vol. 180, pp. 231-266, 1987.
- [42] S. Pope, *Turbulent Flows*, Cambridge University Press, 2000.
- [43] R. Stull, *An Introduction to Boundary Layer Meteorology*, Kluwer Academic Publishers, Dordrecht, Boston and London, pp.1-666, 1988.
- [44] W. Bos, “Production and dissipation of kinetic energy in grid turbulence,” *Physical Review Fluids*, vol. 104607, pp. 1-26, DOI: 10.1103/PhysRevFluids.5.104607, 2020.
- [45] M. Anand and S. Pope, “Diffusion behind a line source in grid turbulence,” in *Turbulent shear flows*, vol. 4, Berlin, Springer-Verlag, edited by Bradbury L.J.S., Durst F., Launder B.E., Schmidt F.W., Whitelaw J.H., 1985, p. 46–61.
- [46] B. Sawford, “Micro-Mixing modelling of scalar fluctuations for plumes in homogeneous turbulence,” *Flow, Turbulence and Combustion*, vol. 72, pp. 133-160, 2004.
- [47] J. Fackrell and A. Robins, “Concentration fluctuations and fluxes in plumes from point sources in a turbulent boundary layer,” *Journal of Fluid Mechanics*, vol. 117, p. 1–26, 1982.
- [48] A. Amicarelli, G. Leuzzi, P. Monti and D. Thomson, “A comparison between IECM and IEM Lagrangian models,” *International Journal of Environment and Pollution*, vol. 44, no. 1/2/3/4, pp. 324-331, 2011.
- [49] R. Secchi, *Sviluppo di un piano cottura per uso domestico alimentabile ad idrogeno e commercializzabile in ambito europeo*, Florence: Università degli studi di Firenze, PhD thesis, 2013.
- [50] L. Fang, L. Li, J. Guo, Y. Liu and X. Huang, “Time scale of directional change of active Brownian particles,” *Physics Letters A*, vol. 427, no. 127934, p. <https://doi.org/10.1016/j.physleta.2022.127934>, 2022.
- [51] R. Martinuzzi and C. Tropea, “The flow around surface-mounted, prismatic obstacles placed in a fully developed channel flow,” *J. Fluids Eng.*, vol. 115, pp. 85-92, <https://doi.org/10.1115/1.2910118>, 1993.
- [52] I. Mavroidis, R. Griffiths and D. Hall, “Field and wind tunnel investigations of plume dispersion around single surface obstacles,” *Atmospheric Environment*, vol. 37, pp. 2903-2918, DOI: 10.1016/S1352-2310(03)00300-5, 2003.
- [53] M. Atzori, S. Chibbaro, C. Duwig and L. Brandt, “LES and RANS calculations of particle dispersion behind a wall-mounted cubic obstacle,” *International Journal of Multiphase Flow*, vol. 151, p. <https://doi.org/10.1016/j.ijmultiphaseflow.2022.104037>, 2022.
- [54] J. Jeong and F. Hussain, “On the identification of a vortex,” *Journal of Fluid Mechanics*, vol. 285, pp. 69-94, DOI: 10.1017/S0022112095000462, 1995.
- [55] A. Amicarelli, “A Lagrangian RANS CFD-SPH code for turbulent flows with pollutant transport and applications to Outdoor/Indoor/Duct Air Quality,” pp. paper preprint, protocol RS2401, pp.1-30, 2024.